Provided for non-commercial research and education use.
Not for reproduction, distribution or commercial use.

(This is a sample cover image for this issue. The actual cover is not yet available at this time.)

This article appeared in a journal published by Elsevier. The attached copy is furnished to the author for internal non-commercial research and education use, including for instruction at the authors institution and sharing with colleagues.

Other uses, including reproduction and distribution, or selling or licensing copies, or posting to personal, institutional or third party websites are prohibited.

In most cases authors are permitted to post their version of the article (e.g. in Word or Tex form) to their personal website or institutional repository. Authors requiring further information regarding Elsevier's archiving and manuscript policies are encouraged to visit:

http://www.elsevier.com/copyright

Author's personal copy

Remote Sensing of Environment 118 (2012) 21–39

Contents lists available at SciVerse ScienceDirect

Remote Sensing of Environment

journal homepage: www.elsevier.com/locate/rse

A novel algorithm for land use and land cover classification using RADARSAT-2 polarimetric SAR data☆

Zhixin Qi [a,]*, Anthony Gar-On Yeh [a], Xia Li [b], Zheng Lin [b]

[a] Department of Urban Planning and Design, The University of Hong Kong, Pokfulam Road, Hong Kong SAR, P.R. China
[b] School of Geography and Planning, Sun Yat-sen University, 135 West Xingang Road, Guangzhou 510275, P.R. China

ARTICLE INFO

Article history:
Received 1 June 2011
Received in revised form 14 October 2011
Accepted 7 November 2011
Available online xxxx

Keywords:
Land use classification
Polarimetric SAR
Polarimetric interferometric SAR
Object-oriented method
Decision tree

ABSTRACT

This study proposes a new four-component algorithm for land use and land cover (LULC) classification using RADARSAT-2 polarimetric SAR (PolSAR) data. These four components are polarimetric decomposition, PolSAR interferometry, object-oriented image analysis, and decision tree algorithms. First, polarimetric decomposition can be used to support the classification of PolSAR data. It is aimed at extracting polarimetric parameters related to the physical scattering mechanisms of the observed objects. Second, PolSAR interferometry is used to extract polarimetric interferometric information to support LULC classification. Third, the main purposes of object-oriented image analysis are delineating image objects, as well as extracting various textural and spatial features from image objects to improve classification accuracy. Finally, a decision tree algorithm provides an efficient way to select features and implement classification. A comparison between the proposed method and the Wishart supervised classification which is based on the coherency matrix was made to test the performance of the proposed method. The overall accuracy of the proposed method was 86.64%, whereas that of the Wishart supervised classification was 69.66%. The kappa value of the proposed method was 0.84, much higher than that of the Wishart supervised classification, which exhibited a kappa value of 0.65. The results indicate that the proposed method exhibits much better performance than the Wishart supervised classification for LULC classification. Further investigation was carried out on the respective contribution of the four components to LULC classification using RADARSAT-2 PolSAR data, and it indicates that all the four components have important contribution to the classification. Polarimetric information has significant implications for identifying different vegetation types and distinguishing between vegetation and urban/built-up. The polarimetric interferometric information extracted from repeat-pass RADARSAT-2 images is important in reducing the confusion between urban/built-up and vegetation and that between barren/sparsely vegetated land and vegetation. Object-oriented image analysis is very helpful in reducing the effect of speckle in PolSAR images by implementing classification based on image objects, and the textural information extracted from image objects is helpful in distinguishing between water and lawn. The decision tree algorithm can achieve higher classification accuracy than the nearest neighbor classification implemented using Definiens Developer 7.0, and the accuracy of the decision tree algorithm is similar with that of the support vector classification which is implemented based on the features selected using genetic algorithms. Compared with the nearest neighbor and support vector classification, the decision tree algorithm is more efficient to select features and implement classification. Furthermore, the decision tree algorithm can provide clear classification rules that can be easily interpreted based on the physical meaning of the features used in the classification. This can provide physical insight for LULC classification using PolSAR data.

© 2011 Elsevier Inc. All rights reserved.

1. Introduction

Timely land use and land cover (LULC) information is essential for urban planning and management. With the rapid growth of China's economy in the last two decades, the demand for land resources for industrial and residential purposes has imposed increasing pressure on the management of agricultural and reserved lands. The insufficiency of available land has caused land prices to soar. As a result, many illegal land development schemes are emerging in some of

☆ This paper is an original work and is currently not being considered for publication in any other journal.

* Corresponding author at: Department of Urban Planning and Design, Room 836, Knowles Building, The University of Hong Kong, Pokfulam Road, Hong Kong, China. Tel.: +852 2857 8644; fax: +852 2559 0468.
E-mail addresses: qizhixin@hku.hk (Z. Qi), hdxugoy@hkucc.hku.hk (A.G.-O. Yeh), lixia@mail.sysu.edu.cn (X. Li), linzheng007@163.com (Z. Lin).

0034-4257/$ – see front matter © 2011 Elsevier Inc. All rights reserved.
doi:10.1016/j.rse.2011.11.001

Author's personal copy

China's rapidly developing regions, such as the Pearl River Delta (PRD). Some illegal land development projects have caused irreversible environmental problems, such as forest degradation, soil erosion, and adverse effects on species diversity (Yeh & Li, 1996). Timely LULC information is important for local governments to create policies that will enable the maintenance of good balance between land development and environmental protection. Remote sensing data obtained from different optical sensors have been commonly used to characterize and quantify LULC information (Saatchi et al., 1997; Roberts et al., 2003; Thenkabail et al., 2005). However, conventional optical remote sensing is limited by weather conditions. Difficulties are encountered in collecting timely LULC information in tropical regions (e.g., PRD) that are characterized by frequent cloud cover. Radar remote sensing, which is not affected by clouds, is therefore an effective tool for extracting timely LULC information in such regions.

Early studies that have used radar remote sensing to investigate LULC information have been mainly carried out using the space shuttle SIR-C/X-SAR (Saatchi et al., 1997; Pierce et al., 1998). Although the results of these studies are positive, the airborne radar imagery systems are only occasionally launched to collect experimental data within a very short period. The regular investigation of timely LULC information using radar remote sensing has become practical after some operational orbital radar systems with SAR, such as the ERS-1 and ERS-2, JERS-1, and RADARSAT-1, were made available for regular data collection. However, most of the existing orbital SAR systems are single-frequency types and may create confusion during the separation and mapping of LULC classes; this confusion stems from the limited information obtained by single-frequency systems (Ulaby et al., 1986; Li & Yeh, 2004).

To overcome the difficulty presented by single-frequency SAR data, some researchers utilized polarimetric SAR (PolSAR) data to investigate LULC information (Pierce et al., 1994; Du & Lee, 1996; Lee et al., 2001; Freitas et al., 2008). The results show that PolSAR measurements achieve better classification results than does single-polarization SAR. The classification of PolSAR images has become an important research topic since PolSAR images have been made available through ENVISAT ASAR, ALOS PALSAR, and RADARSAT-2. Many classification methods for PolSAR data have been explored (Rignot et al., 1992; Chen et al., 1996; Barnes & Burki, 2006; Alberga, 2007; Shimoni et al., 2009). Recently, some polarimetric decomposition theorems have been introduced (Cloude & Pottier, 1996; Freeman & Durden, 1998; Yang et al., 1998; Cameron & Rais, 2006), and classification methods based on decomposition results have been explored (Cloude & Pottier, 1997; Lee et al., 1999a; Pottier & Lee, 2000; Ferro-Famil et al., 2001). The polarimetric parameters extracted using different polarimetric decomposition methods are related to the physical properties of natural media, and can thus be used to classify LULC types. In addition to polarimetric information, polarimetric interferometric SAR (PolInSAR) provides polarimetric interferometric information related to the structure and complexity of the observed objects. Substantial improvements in LULC classification can be achieved by combining polarimetric and polarimetric interferometric information (Crawford et al., 1999; Gamba & Houshmand, 1999; Shimoni et al., 2009). Moreover, some studies have indicated that the fusion of physical and textural information derived from various SAR polarizations is helpful in improving classification results (Borghys et al., 2006). Thus far, however, most of the classification methods are pixel-based in using PolSAR data, especially RADARSAT-2 data. Utilizing the textural and spatial information of PolSAR images through pixel-based methods is a difficult approach. Furthermore, the results of pixel-based methods are insufficient for extracting objects of interest and expediently updating geographical information system databases.

Object-oriented image analysis has been increasingly used for the classification of remote sensing data (Geneletti & Gorte, 2003; Gao et al., 2006; Li et al., 2008; Li et al., 2009; Watts et al., 2009). It enables the acquisition of a variety of textural and spatial features for improving the accuracy of remote sensing classification by delineating objects from remote sensing images. A feature is an attribute that represents certain information concerning objects of interest. Given that regions in an image provide considerably more information than do pixels, many different features for measuring color, shape, and texture of the associated regions are used (Benz et al., 2004). Furthermore, image objects are less affected by speckle in SAR images than in pixels. However, with the addition of polarimetric, interferometric, textural, and spatial information, hundreds of features can potentially be incorporated into the object-oriented classification of PolSAR images. Therefore, feature selection presents a problem in the object-oriented classification of PolSAR data. Using all available features in classification is improper because computation is intensive and some features may degrade classification performance.

Decision tree algorithms can be used to solve the problem of feature selection in object-oriented classification (Lawrence & Wright, 2001). By examining the effects of every input feature to determine every split in a final tree, decision tree algorithms can efficiently select the most important features that achieve the best classification result. Some studies have shown that decision trees can provide an accurate and efficient method for the classification of remote sensing images (Swain & Hauska, 1977; Friedl & Brodley, 1997; McIver & Friedl, 2002). The improvement achieved by the integration of object-oriented image analysis and decision tree algorithms for the classification of multi-spectral optical data has been demonstrated (Watts et al., 2009). However, there is still a general lack of studies on the integration of these two methods for the classification of PolSAR data.

The objective of the current study is to examine a new method for LULC classification using RADARSAT-2 PolSAR data. The proposed method is based on the integration of polarimetric decomposition, PolSAR interferometry, object-oriented image analysis, and decision tree algorithms. To begin with, 66 polarimetric parameters were extracted using different polarimetric decomposition methods, and five polarimetric interferometric parameters were extracted using PolSAR interferometry techniques. Next, the polarimetric and polarimetric interferometric parameters were combined with the elements of the backscattering and coherency matrices to form a multichannel image. During the object-oriented image analysis, image objects were delineated by implementing multi-resolution segmentation on the Pauli RGB composition image of RADARSAT-2 PolSAR data. Meanwhile, a total of 1897 features were extracted from the multichannel image for each image object. After this, a decision tree algorithm was used to select features and create a decision tree for the LULC classification. Finally, the LULC classification was implemented using the constructed decision tree.

2. Study site and data

The study site is located in Panyu District of Guangzhou City in Southern China (Fig. 1). Panyu lies at the heart of the PRD, and has a total land area of 1314 km^2 as well as a population of 926,542. This district was an agricultural area before the economic reform in 1978, but has been transformed recently into a rapidly urbanized area. Since Panyu became a district of Guangzhou in July 2000, intensive land development has been implemented to provide housing to the residents of Guangzhou City. Huge profits have been generated through property development, which resulted in the increase in land speculation activities and illegal land development. Timely and accurate LULC information is important for the local government to create management policies for the control and prevention of illegal development at its early stage.

RADARSAT-2 is the world's most advanced commercial C-band SAR satellite. It is designed with significant and powerful technical advancements, one of which is multi-polarization. RADARSAT-2 can

Author's personal copy

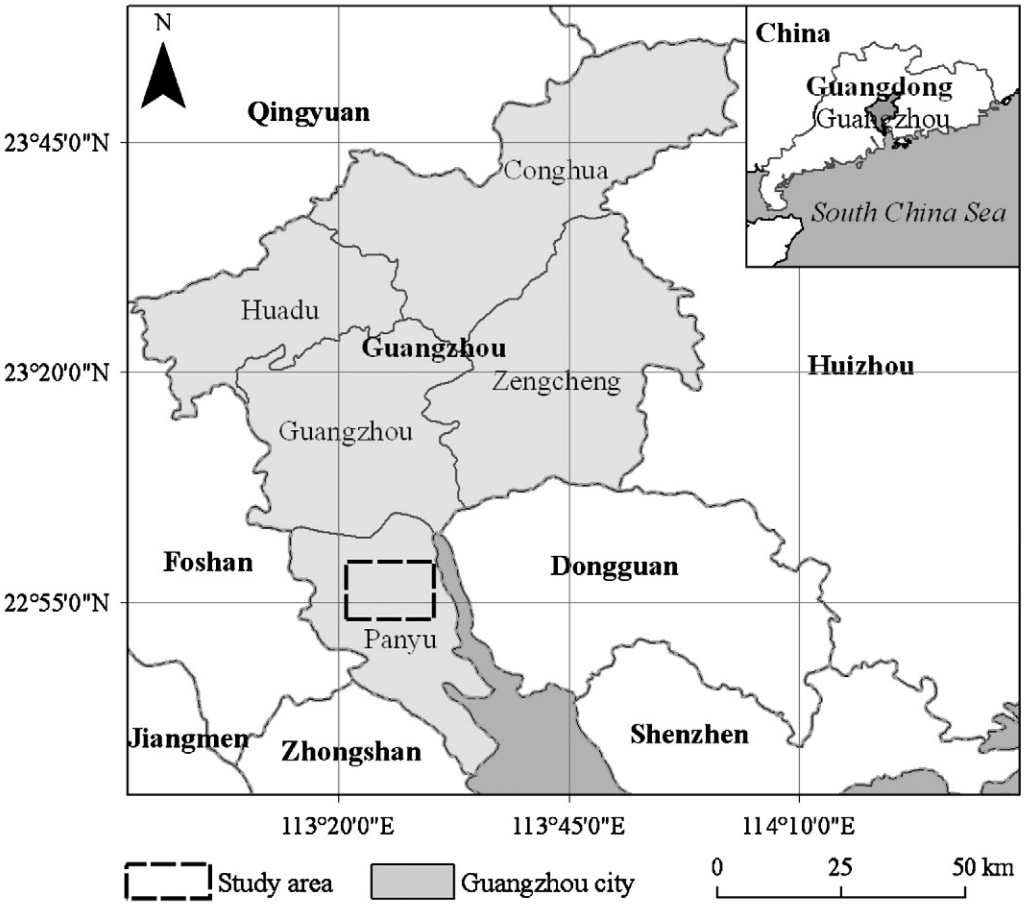

Fig. 1. Study site for LULC classification using RADARSAT-2 PolSAR data in Guangzhou.

transmit horizontal (H) and vertical (V) polarizations depending on the selected mode. Each scattering element (HH, VV, HV, and VH) has varying sensitivities to different surface characteristics and properties, thereby helping improve the discrimination among LULC types. Two repeat-pass RADARSAT-2 Fine Quad-Pol images (Single Look Complex), acquired on 21 March 2009 (Fig. 2a) and 14 April 2009, respectively, were used for the LULC classification in this study. The images have a full polarization of HH, HV, VH, and VV, a resolution of 5.2×7.6 m, and an incidence angle of 31.5°. The multitemporal information of the images was not considered in this work, and the image acquired on 21 March 2009 was used to provide all the information for the LULC classification, except for the polarimetric interferometric information that was extracted from the two images.

LULC classes in the study area can be summarized into seven categories: urban/built-up (UB), water (W), barren/sparsely vegetated land (BS), forest (F), lawn (L), banana (B), and cropland/natural vegetation (CN) (Fig. 3). The field investigations were carried out simultaneously with the acquisitions of the images to collect ground truth. An ALOS image of the 10-m multispectral bands, acquired on 31 November 2008, was used as a reference map to facilitate the collection of ground truth in the field investigations (Fig. 2b). In the field investigations, a total of 727 field plots were selected across the typical LULC classes using a clustered sampling approach (McCoy, 2005) (Fig. 4). In a terrain with poor access, this sampling approach enables the use of most of the accessible sites. A GPS was used to record the coordinates of these field plots. On the basis of the experience with multinomial distribution (Congalton & Green, 2009), we collected a minimum of 50 samples for each category. The sampling size per field plot in the images ranged from 39 to 603 pixels; this range was determined using the ground coverage in the photos taken during the fieldwork. The collected field plots were divided into two groups for training and validation. There are 357 plots in the training group and 370 plots in the validation group. The first group was used to select features and create a decision tree for classification, while the second group was used to verify the results of the classification. The number of the plots and pixels selected for each LULC class in the training and validation groups is shown in Table 1.

3. Methodology

The methodology is based on the integration of polarimetric decomposition, PolSAR interferometry, object-oriented image analysis, and decision tree algorithms. Before any further analysis, the RADARSAT-2 PolSAR data was filtered using the 5×5 refined Lee PolSAR speckle filter (Lee et al., 1999b). This speckle filter effectively preserves polarimetric information and retains subtle details while reducing the speckle effect in homogeneous areas.

3.1. Polarimetric decomposition

A distinct characteristic of a PolSAR system is the utilization of polarized waves. The observed polarimetric signatures of the electric field backscattered by the scene depend strongly on the scattering properties of the image objects. In comparison with conventional single-polarization SAR, the inclusion of SAR polarimetry allows for the discrimination of different types of scattering mechanisms that leads to a significant improvement in the quality of classification results. Polarimetric decomposition techniques aim to separate a received signal by the radar as the combination of the scattering responses of simpler objects presenting an easier physical interpretation, which can be used to extract the corresponding target types in images.

Author's personal copy

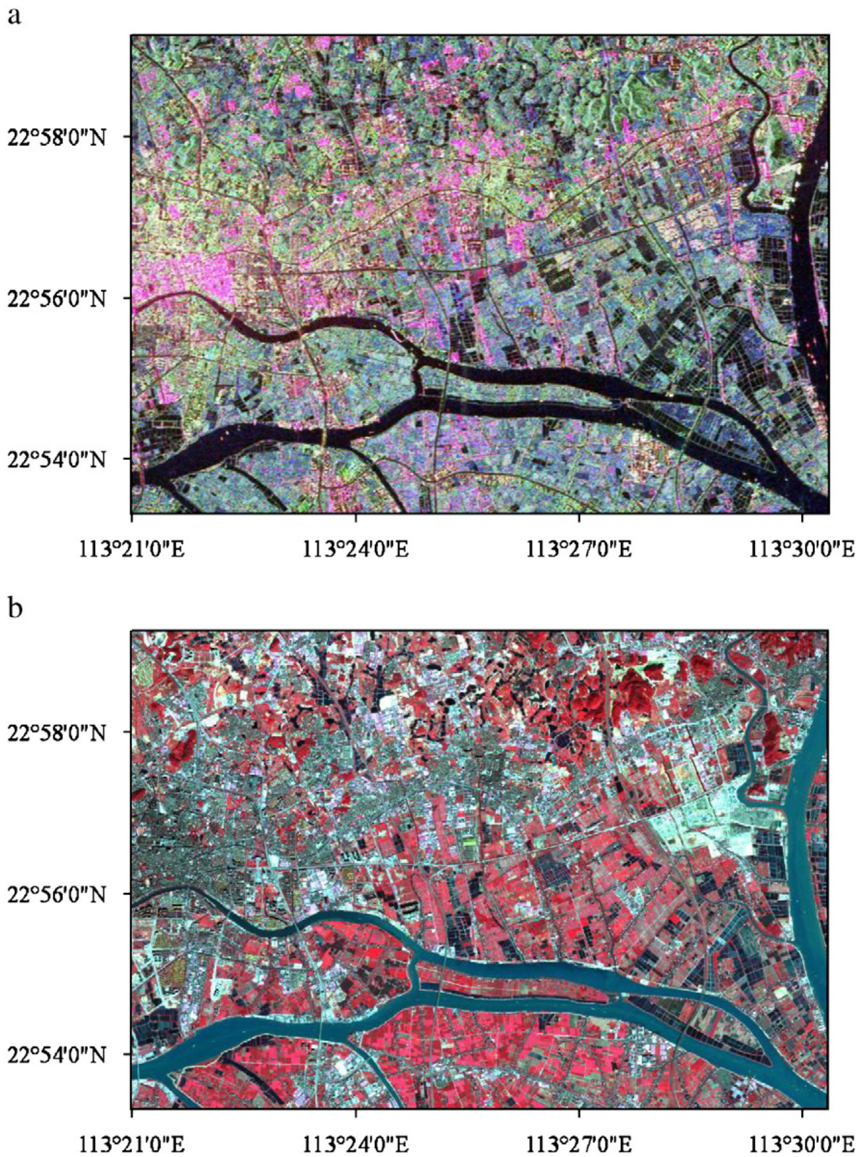

Fig. 2. (a) RADARSAT-2 PolSAR image acquired on 21 March 2009 (Pauli RGB composition), (b) ALOS image acquired on 31 November 2008.

Fig. 3. Typical LULC classes in the study site.

Author's personal copy

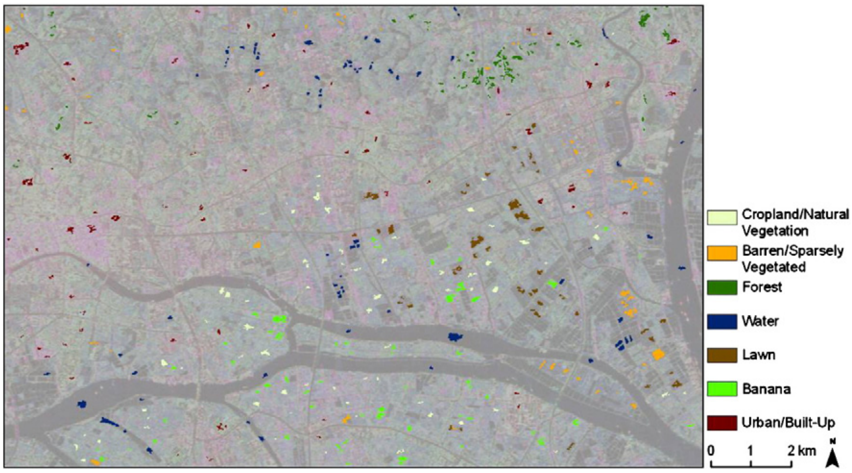

Fig. 4. Collected filed plots across typical LULC classes in the study site.

The Pauli decomposition is a well-known decomposition method commonly used for PolSAR data (Cloude & Pottier, 1996). In the Pauli decomposition, backscattering matrix ***S*** is expressed as the complex sum of the Pauli matrices.

$$S = \begin{bmatrix} S_{hh} & S_{hv} \\ S_{vh} & S_{vv} \end{bmatrix} = \frac{a}{\sqrt{2}}\begin{bmatrix} 1 & 0 \\ 0 & 1 \end{bmatrix} + \frac{b}{\sqrt{2}}\begin{bmatrix} 1 & 0 \\ 0 & -1 \end{bmatrix} + \frac{c}{\sqrt{2}}\begin{bmatrix} 0 & 1 \\ 1 & 0 \end{bmatrix} + \frac{d}{\sqrt{2}}\begin{bmatrix} 1 & -j \\ j & 1 \end{bmatrix} \quad (1)$$

where a, b, c, and d are all complex and are given by:

$$a = \frac{S_{hh}+S_{vv}}{\sqrt{2}} \quad b = \frac{S_{hh}-S_{vv}}{\sqrt{2}} \quad c = \frac{S_{hv}+S_{vh}}{\sqrt{2}} \quad d = j\frac{S_{hv}-S_{vh}}{\sqrt{2}} \quad (2)$$

If the transmit and receive antennas coincide, the backscattering matrix may be symmetric, with $S_{hv}=S_{vh}$, and the Pauli matrix basis can be reduced to the first three matrices. The polarimetric parameters from the Pauli decomposition are associated for three elementary scattering mechanisms: a stands for single or odd-bounce scattering, b represents double or even-bounce scattering, and c denotes volume scattering. The total received power from the four polarimetric channels of the backscattering matrix is referred to as "span". Eq. (3) shows that the span of ***S*** can be obtained as follows:

$$Span = |S_{hh}|^2 + 2|S_{hv}|^2 + |S_{vv}|^2 = |a|^2 + |b|^2 + |c|^2 \quad (3)$$

Thus, the Pauli decomposition of the backscattering matrix is often employed to represent all the polarimetric information in a PolSAR image. As shown in Fig. 2a, a Pauli RGB composition image can be formed with intensities $|a|^2$ (blue), $|b|^2$ (red), and $|c|^2$ (green), which correspond to clear physical scattering mechanisms. The Pauli RGB composition image has become the standard for PolSAR image display and has often been used for visual interpretation.

Table 1
Number of the plots and pixels selected for each LULC class in the training and validation groups.

Class	Training		Validation	
	Plots	Pixels	Plots	Pixels
Banana	50	8902	50	9423
Urban/built-up	55	9219	52	9137
Cropland/natural vegetation	50	8510	63	9060
Barren/sparsely vegetated land	50	9962	50	8734
Forest	51	7453	55	8476
Lawn	50	9203	50	9871
Water	51	10,900	50	9542
Total	357	64,149	370	64,243

The backscattering matrix elements can be arranged into a vector: $\boldsymbol{k} = 0.707\,[S_{hh}+S_{vv}, S_{hh}-S_{vv}, 2S_{hv}]$, with the tree elements referred to as the Pauli components of the signal. The 3×3 coherency matrix $\boldsymbol{T_3}$ is defined as the expected value of $\boldsymbol{kk}^{*\mathrm{T}}$ (Lee & Pottier, 2009).

$$T_3 = \begin{bmatrix} T_{11} & T_{12} & T_{13} \\ T_{12}^* & T_{22} & T_{23} \\ T_{13}^* & T_{23}^* & T_{33} \end{bmatrix} = \frac{1}{2}\begin{bmatrix} |S_{hh}+S_{vv}|^2 & (S_{hh}+S_{vv})(S_{hh}-S_{vv})^* & 2(S_{hh}+S_{vv})S_{hv}^* \\ (S_{hh}-S_{vv})(S_{hh}+S_{vv})^* & |S_{hh}-S_{vv}|^2 & 2(S_{hh}-S_{vv})S_{hv}^* \\ 2S_{hv}(S_{hh}+S_{vv})^* & 2S_{hv}(S_{hh}-S_{vv})^* & 4|S_{hv}|^2 \end{bmatrix} \quad (4)$$

where * denotes the conjugate and || denotes the module. Coherency matrix $\boldsymbol{T_3}$ is a close relative of covariance matrix $\boldsymbol{C_3}$ (Lee & Pottier, 2009). They contain the same information, but this information comes in different forms.

In addition to the Pauli decomposition, many other decomposition methods have been proposed to express the measured backscattering matrix ***S*** as a combination of the scattering responses of simpler objects, or to separate coherency matrix $\boldsymbol{T_3}$ or covariance matrix $\boldsymbol{C_3}$ as the combination of second-order descriptors corresponding to simpler or canonical objects presented as an easier physical interpretation (Cloude & Pottier, 1996). Classification methods based on polarimetric decomposition results have also been explored (Cloude & Pottier, 1997; Lee et al., 1999a; Pottier & Lee, 2000; Ferro-Famil et al., 2001). However, most of these methods merely focused on one polarimetric decomposition method. Shimoni et al. (2009) stated that different polarimetric decomposition methods should be used for land cover classification because they emphasize different land cover types. In the present study, all the polarimetric decomposition methods provided by the PolSARPro_v4.1.5 software (López-Martínez et al., 2005) were used to extract polarimetric parameters for classification support. These decomposition methods are the Pauli (Cloude & Pottier, 1996), Barnes (Barnes, 1988), Huynen (Huynen, 1970), Cloude (Cloude, 1985), Holm (Holm & Barnes, 1988), H/A/Alpha (Cloude & Pottier, 1997), Freeman 2 Components (Freeman, 2007), Freeman 3 Components (Freeman & Durden, 1998), Van Zyl (Vanzyl, 1993), Neumann (Neumann et al., 2009), Krogager (Krogager, 1990), Yamaguchi (Yamaguchi et al., 2005), and Touzi (Touzi, 2007) methods. The RGB composition images that present some of these decompositions are shown in Fig. 5.

Aside from the primary polarimetric parameters extracted using different polarimetric decomposition methods, some secondary

Author's personal copy

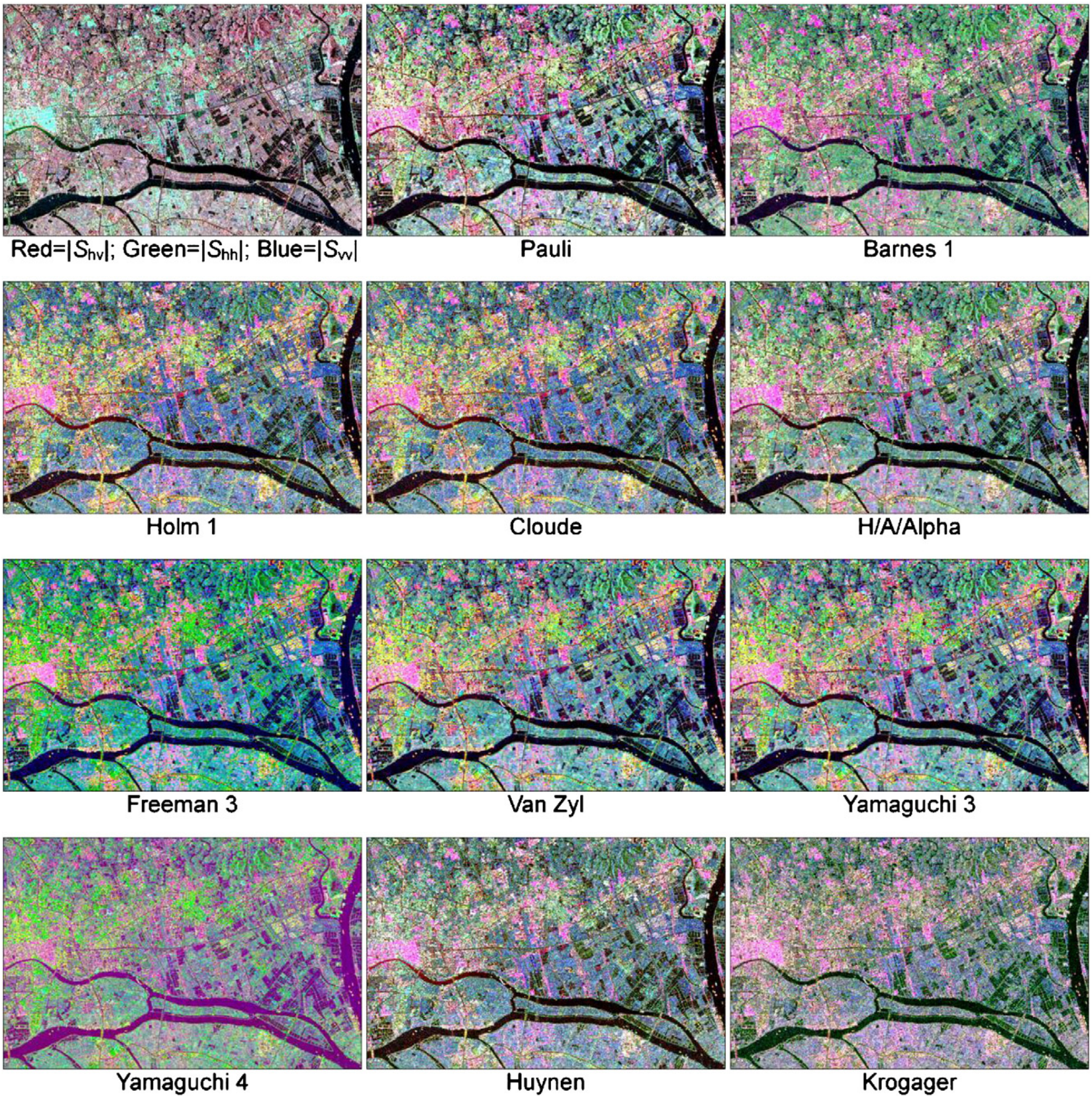

Fig. 5. RGB composition images presenting different polarimetric decompositions.

polarimetric parameters are defined as a function of the primary polarimetric parameters to simplify the analysis of physical information in some decomposition methods, such as H/A/Alpha decomposition. These secondary polarimetric parameters were also calculated and used in the current work as the complementary for the primary parameters. After in-depth research on the suitability and usability of the extracted polarimetric parameters, 66 polarimetric parameters were selected for the LULC classification (Table 2). The descriptors used in PolSARPro_v4.1.5 for these polarimetric parameters were adopted. The calculation and the physical interpretation of these polarimetric parameters can be referred to in the study of Lee and Pottier (2009).

3.2. PolSAR interferometry for LULC classification

A six-element complex scattering target vector $\boldsymbol{k_6}$ can be formed by stacking two Pauli-scattering target vectors $\boldsymbol{k_1}$ and $\boldsymbol{k_2}$ of fully polarimetric interferometric SAR system images from two slightly different look angles in a repeat-pass interferometric configuration (Lee & Pottier, 2009).

$$k_6 = \begin{bmatrix} k_1 \\ k_2 \end{bmatrix} = \frac{1}{\sqrt{2}} \begin{bmatrix} S_{hh1} + S_{vv1} \\ S_{hh1} - S_{vv1} \\ 2S_{hv1} \\ S_{hh2} + S_{vv2} \\ S_{hh2} - S_{vv2} \\ 2S_{hv2} \end{bmatrix} \tag{5}$$

The 6×6 Pauli coherency $\boldsymbol{T_6}$ matrix is defined as the outer product of the associated target vector with its conjugate transpose (Lee & Pottier, 2009).

$$T_6 = \left\langle k_6 \cdot k_6^{*T} \right\rangle = \begin{bmatrix} \left\langle k_1 \cdot k_1^{*T} \right\rangle & \left\langle k_1 \cdot k_2^{*T} \right\rangle \\ \left\langle k_2 \cdot k_1^{*T} \right\rangle & \left\langle k_2 \cdot k_2^{*T} \right\rangle \end{bmatrix} = \begin{bmatrix} T_{11} & \Omega_{12} \\ \Omega_{12}^{*T} & T_{22} \end{bmatrix} \tag{6}$$

Author's personal copy

Table 2
Polarimetric parameters extracted using different polarimetric decomposition methods for LULC classification using RADARSAT-2 PolSAR data.

Decomposition method	Polarimetric parameter		
Pauli	Pauli_*a*	Pauli_*b*	Pauli_*c*
Barnes1	Barnes1_T_{11}	Barnes1_T_{22}	Barnes1_T_{33}
Barnes2	Barnes2_T_{11}	Barnes2_T_{22}	Barnes2_T_{33}
Huynen	Huynen_T_{11}	Huynen_T_{22}	Huynen_T_{33}
Cloude	Cloude_T_{11}	Cloude_T_{22}	Cloude_T_{33}
Holm1	Holm1_T_{11}	Holm1_T_{22}	Holm1_T_{33}
Holm2	Holm2_T_{11}	Holm2_T_{22}	Holm2_T_{33}
H/A/Alpha	H/A/A_T_{11}	H/A/A_T_{22}	H/A/A_T_{33}
	Entropy(H)	PedestalHeight (PH)	ShannonEntropy (SE)
	DERD	PolarizationAsymmetry (PA)	PolarizationFraction (PF)
	SERD	RadarVegetationIndex (RVI)	TargetRandomness (P_R)
	Anisotropy(A)	AlphaAngle($\overline{\alpha}$,α1,α2,α3)	
Freeman2Components	Freeman2_Vol	Freeman2_Ground	
Freeman3Components	Freeman_Vol	Freeman_Odd	Freeman_Dbl
VanZyl3Components	VanZyl3_Vol	VanZyl3_Odd	VanZyl3_Dbl
Yamaguchi3Components	Yamaguchi3_Vol	Yamaguchi3_Odd	Yamaguchi3_Dbl
Yamaguchi4Components	Yamaguchi4_Vol	Yamaguchi4_Odd	Yamaguchi4_Dbl
	Yamaguchi4_Hlx		
Neumann2Components	Neumann_delta_mod	Neumann_delta_pha	
Krogager	Krogager_KS	Krogager_KD	Krogager_KH
Touzi	TSVM_alpha_s	TSVM_alpha_s1	TSVM_alpha_s2
	TSVM_alpha_s3	TSVM_tau_m	TSVM_tau_m1
	TSVM_tau_m2	TSVM_tau_m3	

where $\langle\cdots\rangle$ indicates temporal or spatial ensemble averaging; $\boldsymbol{T_{11}}$ and $\boldsymbol{T_{22}}$ matrices are the conventional polarimetric Hermitian 3×3 complex coherency matrices describing the polarimetric properties for each individual image; and the $\boldsymbol{\Omega}$ matrix is a non-Hermitian 3×3 complex coherency matrix that contains polarimetric and interferometric correlation information between the two targets $\boldsymbol{k_1}$ and $\boldsymbol{k_2}$.

The complex polarimetric interferometric coherence γ as a function of the polarization of the two images is then given by (Papathanassiou & Cloude, 2001):

$$\gamma(w_1, w_2) = \frac{w_1^{*T}\Omega_{12}w_2}{\sqrt{(w_1^{T*}T_{11}w_1)(w_2^{T*}T_{22}w_2)}} \tag{7}$$

where $\boldsymbol{w_1}$ and $\boldsymbol{w_2}$ are two unitary complex vectors that define the polarization of the two images. Papathanassiou and Cloude (2001) calculated three optimum complex polarimetric interferometric coherences – $\gamma_{\mathrm{opt\_1}}$, $\gamma_{\mathrm{opt\_2}}$, and $\gamma_{\mathrm{opt\_3}}$ – by determining the combination of polarizations that yields the highest coherence. To isolate the polarization-dependent component of the optimal coherences, their relative values are defined as:

$$\overline{\gamma}_{opt\_i} = \frac{|\gamma_{opt\_i}|}{\sum_{j=1}^{3}|\gamma_{opt\_j}|} \tag{8}$$

The relative optimal coherence spectrum can be fully described by two parameters, A_1 and A_2 (Ferro-Famil et al., 2001).

$$A_1 = \frac{\overline{\gamma}_{opt\_1} - \overline{\gamma}_{opt\_2}}{\overline{\gamma}_{opt\_1}} \text{ and } A_2 = \frac{\overline{\gamma}_{opt\_1} - \overline{\gamma}_{opt\_3}}{\overline{\gamma}_{opt\_1}} \tag{9}$$

The PCI Geomatica software was used to implement the co-registration of the repeat-pass RADARSAT-2 images. The RADARSAT-2 image package provides a total of 180 tie points that are evenly distributed across the whole image. These tie points tie the line/pixel positions in image coordinates to geographical latitude/longitude and can be used as ground control points (GCP) to register an image to a geocoded target image. We first created a blank geocoded image that has the same resolution of the RADARSAT-2 images and then registered the two RADARSAT-2 images to this geocoded image by using PCI Geomatica based on the tie points. Visual inspection indicates that these two mages have been registered perfectly. Five polarimetric interferometric parameters ($\gamma_{\mathrm{opt\_1}}$, $\gamma_{\mathrm{opt\_2}}$, $\gamma_{\mathrm{opt\_3}}$, A_1, and A_2) were extracted after the co-registration of the two images (Fig. 6). As shown in Fig. 6, there is a strong contrast between urban and nonurban areas in the images of polarimetric interferometric parameters. The repeat cycle of RADARSAT-2 is 24 days, which produces a very strong temporal decorrelation for nonurban areas, such as croplands and natural vegetation. Croplands and natural vegetation are significantly influenced by temporal decorrelation and lose coherence within a few days or weeks as a result of growth, movement of scatterers, and changing moisture conditions. In contrast, within urban/built-up areas, coherence remains high even between image pairs separated by a long time interval. Therefore, the results in Fig. 6 indicate that accurate polarimetric interferometric information can be extracted based on the co-registration of images implemented based on the tie points. To combine polarimetric and polarimetric interferometric information for LULC classification, we merged the polarimetric and polarimetric interferometric parameters with the backscattering matrix elements (S_{hh}, S_{vv}, and S_{hv}) and the coherency matrix elements (T_{11}, T_{12}, T_{13}, T_{22}, T_{23}, and T_{33}) to form a multichannel image. The backscattering matrix elements were filtered by using the 5×5 boxcar filter in PolSARPro_v4.1.5 before the merging of images. The next step was to delineate image objects and extract features from the multichannel image using object-oriented image analysis.

3.3. Object-oriented image analysis for PolSAR images

One way to compensate for the limited information from single-frequency SAR data is to derive more features, such as texture and shape, for the classification of SAR images in addition to the tonal information of pixels. By delineating objects from images, object-oriented image analysis enables the acquisition of a variety of additional textural and spatial features, which are helpful in improving the accuracy of remote sensing classification (Benz et al., 2004). In this study, the object-oriented package Definiens Developer 7.0 (Baatz et al., 2004) was used to implement the object-oriented image analysis of PolSAR images.

The multi-resolution segmentation module provided by Definiens Developer 7.0 was used to perform object delineation based on shape and color homogeneity. Multi-resolution segmentation is a bottom-up region-merging technique that begins with single-pixel objects.

Author's personal copy

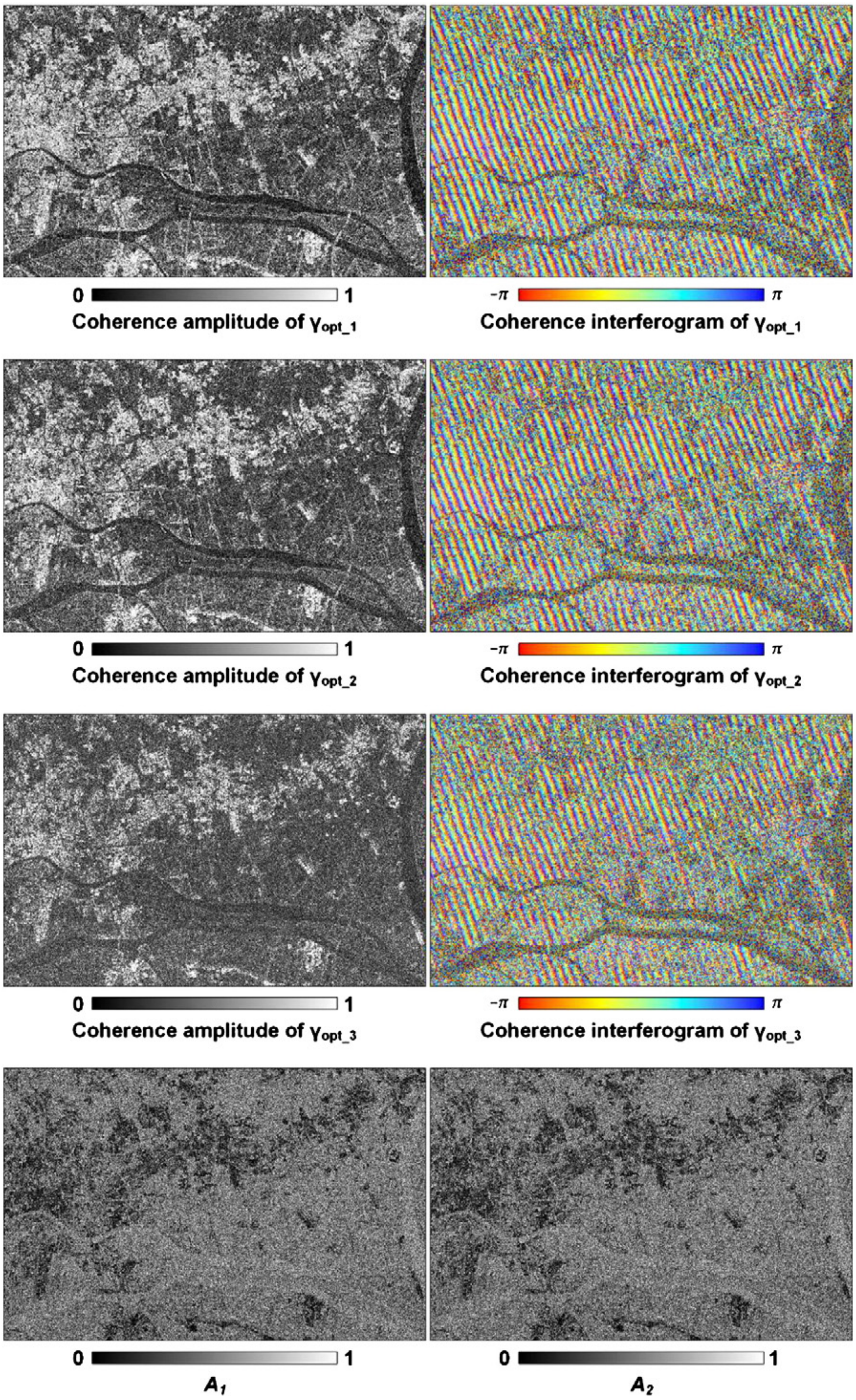

Fig. 6. Polarimetric interferometric parameters extracted using PolSAR interferometry techniques for LULC classification.

During the region-merging process, smaller image objects are merged into larger ones, and a heuristic optimization procedure is used to minimize the weighted heterogeneity of the resultant image objects. Heterogeneity is determined using the standard deviation of color properties and their shapes as basis. The merging of a pair of adjacent image objects increases heterogeneity. The process will stop if the growth exceeds the threshold defined by a scale parameter.

The multichannel image consists of as many as 80 image channels; thus, it is necessary to select appropriate image channels for image segmentation. Using all the channels for image segmentation is improper given that some polarimetric or polarimetric interferometric parameters may degrade segmentation results because some of these parameters may have large noise. Although the backscattering and coherency matrices were filtered, there was still considerable noise in some polarimetric or polarimetric interferometric parameters that were extracted later. For example, large noise exists in pedestal height and complex polarimetric interferometric coherences. Although these parameters represent important information for identifying some LULC types, they are inappropriate for image segmentation because of their poor ability to display the accurate boundaries of land parcels and subtle details. Moreover, the increase in image channels in image segmentation results in much more computation time. Therefore, in this study, the image segmentation was implemented on the Pauli RGB composition image to delineate objects. As previously mentioned, the Pauli RGB composition image has become the standard for PolSAR image display because it can represent all the

Author's personal copy

polarimetric information in a PolSAR image. Furthermore, the Pauli RGB composition image represents clear physical scattering mechanisms, which allow for clear contrast among different LULC types. Given that the three channels of the Pauli RGB composition image correspond to three elementary scattering mechanisms with the same importance, equal weight was assigned to the three channels in the image segmentation.

The scale parameter determines the maximum change in the heterogeneity that may occur when two objects are merged. Adjusting the value of the scale parameter influences the average object size. A higher value leads to larger objects and vice versa. Setting the scale parameter was a heuristic process. Multi-resolution segmentation with different scale parameters was carried out to determine the optimal scale parameter (Fig. 7). The experiment shows that the segmentation with a scale parameter of 20 was good enough for delineating accurate land parcels and retaining subtle details. Image objects became too fragmental at a scale parameter smaller than 20.

Because the multichannel image consists of as many as 80 channels, the number of features that can be extracted from an image object is as high as 1897. These features are the indigenous parameters of Definiens Developer 7.0 (Baatz et al., 2004), and they are listed as four major categories:

- 320 (4×80) indicators related to the statistical values of each object: min, max, mean, and standard deviation of each layer;
- 960 (12×80) indicators related to texture (e.g., gray-level co-occurrence matrix (GLCM) homogeneity, GLCM contrast, GLCM dissimilarity, and GLCM entropy);
- 560 (7×80) indicators related to spatial relationship (e.g., mean difference to neighbors and mean difference to brighter neighbors);
- 57 indicators related to shape (e.g., area, length, number of segments, and main line curvature/length extracted from an image object).

3.4. Object-oriented classification using decision tree algorithms

The determination of the features used in the object-oriented classification of PolSAR data is crucial to the classification result. Decision trees are commonly used to predict the membership of cases or objects in the classes of a categorical dependent variable based on their measurements on one or more predictor variables. Classification accuracies from decision tree classifiers are often greater than the maximum likelihood or linear discriminant function classifiers (Laliberte et al., 2006). Decision tree algorithms have many advantages, which make them suitable for the object-oriented classification of PolSAR data. (1) They are white box models that are simple to understand and interpret. If a final tree is constructed for classification, the classification rules provided by the tree are easily interpreted. (2) By performing univariate splits and examining the effects of predictors one at a time, decision trees are able to handle a variety of types of predictors and require little data preparation. (3) They are robust and perform well with large datasets in a short period. After a final tree is constructed based on a full dimensionality of features, only a calculation of the selected features is needed for classification by this final tree. This makes classification based on a large number of features feasible.

In this study, QUEST (Loh & Shih, 1997; Lim et al., 2000) was used as a decision tree tool to implement the classification. QUEST is a binary-split decision tree algorithm for classification and data mining. Training objects were manually drawn on the Pauli RGB composition image based on the field plots in the training group. After the image segmentation, the training objects were further segmented into a large number of sub-objects. More than 2000 training objects were acquired for the construction of the decision trees. On the basis of the training objects, we constructed a decision tree using QUEST for the LULC classification. To remove the sections of the decision tree that may have arisen from noisy or erroneous data, the tree was

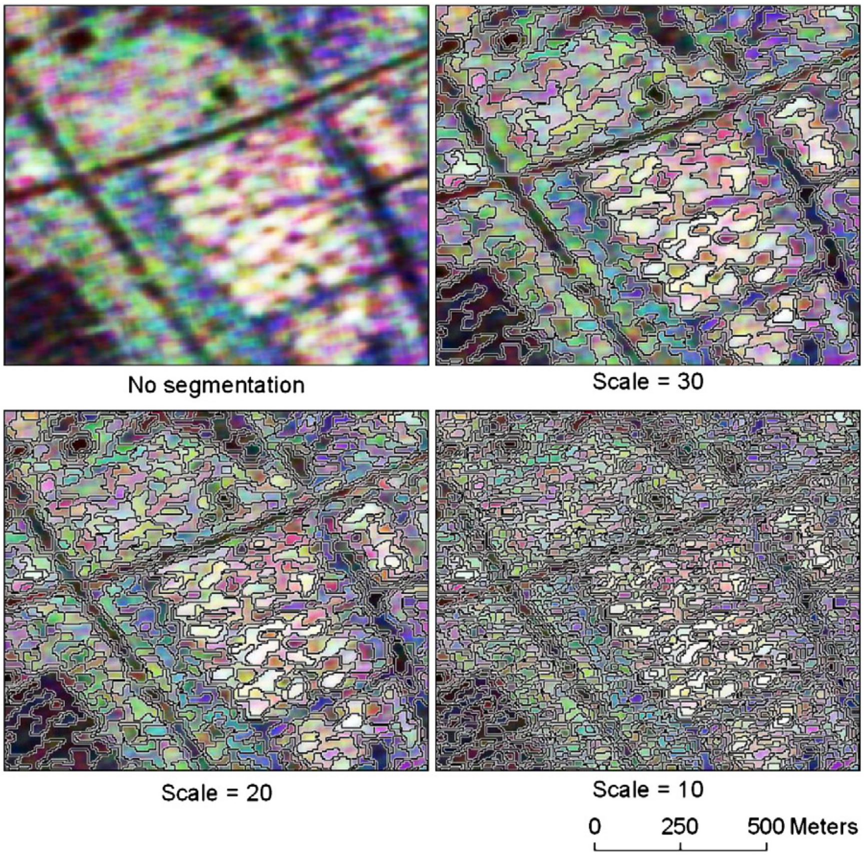

Fig. 7. Determining the optimal scale for the segmentation of the Pauli RGB composition image of RADARSAT-2 PolSAR data.

Author's personal copy

pruned with 10-fold cross-validation and the 1-SE rule; these are common methods for pruning decision trees and are embedded in QUEST. The final tree constructed using QUEST is shown in Fig. 8, and the selected image channels in the final tree are shown in Fig. 9. The detailed features selected in the final tree are listed as follows:

- Layer mean values of T_{11}, T_{13}, T_{23}, Holm2_T$_{22}$, Krogager_KD, PH, VanZyl3_Odd, VanZyl3_Vol, Freeman_Odd, and γ_{opt_2}
  The mean value of an image object that consists of n pixels in channel c is calculated from the value of the pixels (c_i) thus:

$$m_c = \frac{1}{n}\sum_{i=1}^{n} c_i \tag{10}$$

- Standard deviation of Freeman_Vol
  The standard deviation of an image object that consists of n pixels in channel c is calculated from the value of the pixels (c_i).

$$\sigma_c = \sqrt{\frac{1}{n}\left(\sum_{i=1}^{n} c_i^2 - \frac{1}{n}\sum_{i=1}^{n} c_i \sum_{i=1}^{n} c_i\right)} \tag{11}$$

- GLCM entropy of Yamaguchi3_Vol
  GLCM is a tabulation of how often different combinations of pixel gray levels occur in an image.

$$\texttt{GLCM entropy} = \sum_{i,j=0}^{N-1} p_{i,j}\left(-\ln p_{i,j}\right) \tag{12}$$

where i is the row number, j is the column number in the texture calculation cell matrix, N denotes the number of rows or columns of the cell matrix, and $P_{i,j}$ is the normalized value in cells i and j, and is defined as:

$$P_{i,j} = \frac{V_{i,j}}{\sum_{i,j=0}^{N-1} V_{i,j}} \tag{13}$$

where $V_{i,j}$ is the value in cells i and j of the image window. The value for entropy is high if the elements of GLCM are distributed equally, and low if the elements are close to either 0 or 1.

The classification rules of the tree model (Fig. 8) can be interpreted according to the interaction of C-band microwave energy

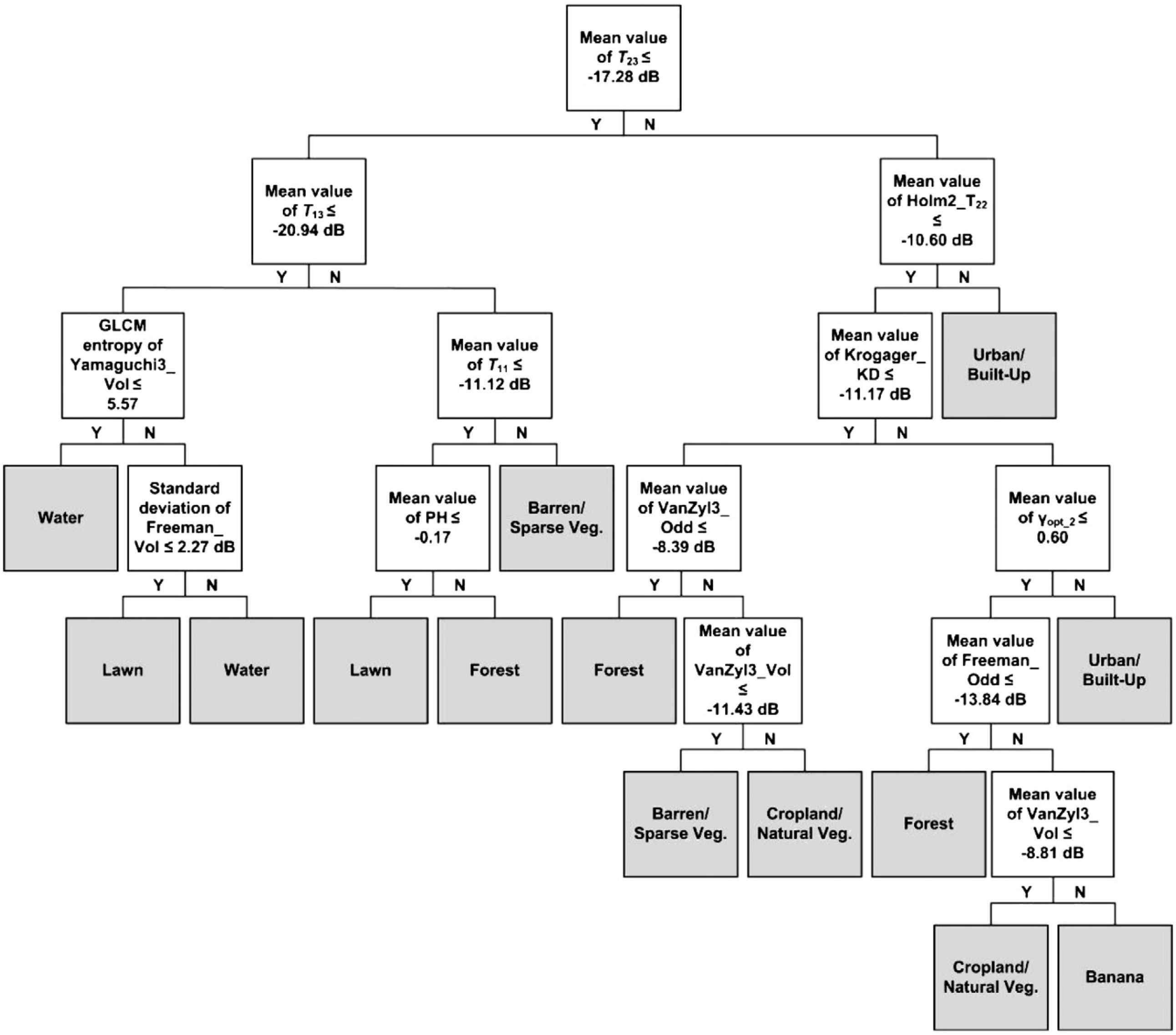

Fig. 8. Decision tree constructed using QUEST for LULC classification using RADARSAT-2 PolSAR data.

Author's personal copy

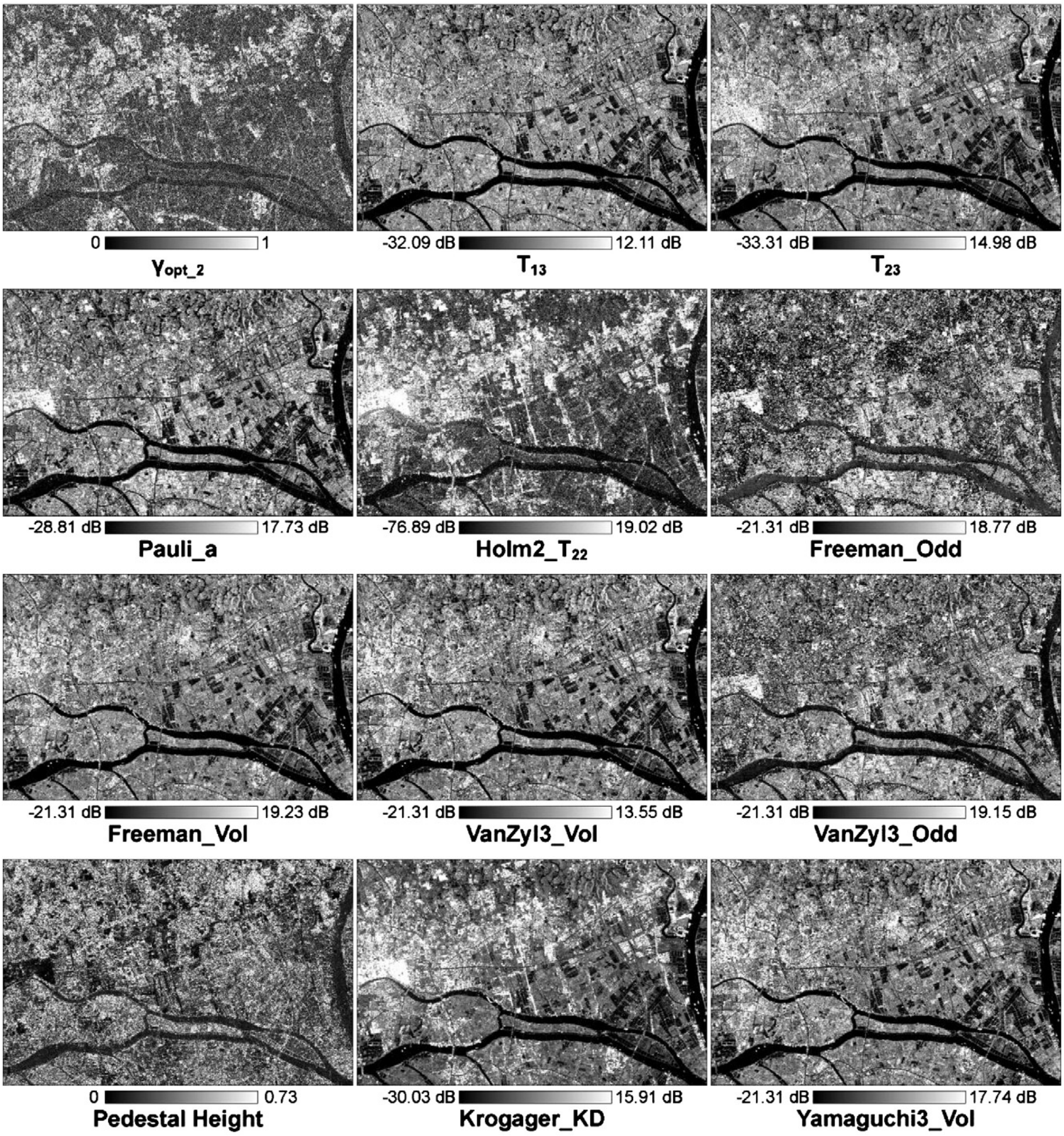

Fig. 9. Image channels selected in the decision tree constructed for LULC classification.

with different LULC classes and the physical meaning of the features used in the classification. The total backscatter from natural vegetation and croplands includes the return scattered from the vegetation canopy (volume scattering), those scattered from the soil beneath (single-bounce scattering), and those from the multiple scattering between the soil and canopy (volume scattering and single or odd-bounce scattering). The total backscatter from forest and banana areas also includes trunk-ground backscatter (double-bounce scattering) and direct backscattering from the trunk (usually small). Given that C-band primarily interacts with the leaves and small and secondary branches, vegetation has the typical characteristics of volume scattering. The main radar return from barren/sparsely vegetated land and lawn is single-bounce scattering, which is greatly influenced by soil surface roughness and moisture content. Water bodies, such as lakes and revisers, are usually distinguished by low return and are presented on radar imagery as dark areas. Urban/built-up areas normally have the typical characteristics of double-bounce scattering. As shown in Fig. 8, at the start, the mean value of T_{23} is used to partition all the samples into two groups. Referring to the physical meaning of the Pauli components, T_{23} ($(S_{hh}-S_{vv})S_{hv}^*$) can be regarded as the sum of double or even-bounce scattering ($S_{hh}-S_{vv}$) and volume scattering (S_{hv}). Therefore, it can be used to distinguish between classes with low radar return, such as water, barren/sparsely vegetated land, and lawn, and classes with strong double-bounce scattering and volume scattering, such as urban/built-up and vegetation. T_{13} ($(S_{hh}+S_{vv})S_{hv}^*$) can be

Author's personal copy

considered as the sum of single or odd-bounce scattering ($S_{hh}+S_{vv}$) and volume scattering (S_{hv}). The classes in the left branch of the mean value of T_{13} are water and lawn (high soil moisture), which have lower single-bounce scattering or volume scattering than barren/sparsely vegetated land, lawn (low soil moisture), and forest in the shadow of mountains in the right branch. The standard deviation of Freeman_Vol and the GLCM entropy of Yamaguchi3_Vol are helpful in distinguishing between water and lawn. In the field investigations, barren land plots were observed in some lawn fields because of the harvest of grass (Fig. 3), which makes the lawn fields more heterogeneous than water. Therefore, the textural information can be used to distinguish between water and lawn. The mean value of T_{11} is used to distinguish barren/sparsely vegetated land from lawn and forest in the shadow of mountains. T_{11} stands for singe or odd-bounce scattering. Compared with lawn and forest in the shadow of mountains, barren/sparsely vegetated land has stronger single-bounce scattering because of low soil moisture and uneven surface. The mean value of PH is helpful in distinguishing between lawn and forest in the shadow of mountains. PH is a polarization signature of measuring randomness in scattering (Durden et al., 1990). The mean value of Holm2_T$_{22}$ is used for distinguishing some urban/built-up areas from vegetation because it corresponds to a high density of pure targets, such as man-made areas. Krogager_KD is interpreted as the power scattered by the diplane-like components of the Krogager decomposition. The classes in the right branch of the mean value of Krogager_KD are urban/built-up and some vegetation types, which provide stronger double-bounce scattering than the vegetation types in the left branch. Although Holm2_T$_{22}$ and Krogager_KD can be used to distinguish most of urban/built-up areas from vegetation, there is still some confusion between urban/built-up and vegetation because of similar scattering mechanism. Generally, buildings have the typical characteristics of double-bounce scattering, and vegetation has the typical characteristics of volume scattering. However, some buildings have specific orientations not aligned in the azimuth direction or have complex structures that backscatter randomly polarized waves thus providing strong volume scattering, and some vegetation, such as banana trees, forests, provide strong double-bounce scattering because of their strong trunks (trunk-ground backscatter). There is also strong double-bounce scattering from some croplands during the irrigation (trunk-water backscatter). The polarimetric interferometric information (γ_{opt_2}) extracted from the repeat-pass RADARSAT-2 images can be used to identify urban/built-up that tends to be confused with vegetation because of the similar scattering mechanisms. The repeat cycle of RADARSAT-2 is 24 days, which produces a very strong temporal decorrelation for vegetation. However, urban/built-up area still has strong correlation in 24 days because of their stable status. Therefore, the contrast between urban/built-up and vegetation in γ_{opt_2} can be used to distinguish between them. Freeman_Odd stands for the contribution of the single or odd-bounce scattering in the Freeman decomposition. There is stronger single or odd-bounce scattering from cropland/natural vegetation and banana than from forests because less microwave energy penetrates the crown layer of forests and interacts with the ground. Therefore, the mean value of Freeman_Odd is used to distinguish forest from cropland/natural vegetation and banana. Vanzyl3_Vol corresponds to the contribution of the volume scattering in the van Zyl decomposition. Given that banana provides more return scattered from its dense canopy than cropland/natural vegetation, the mean value of Vanzyl3_Vol can be used to distinguish between banana and cropland/natural vegetation. VanZyl3_Odd corresponds to the contribution of the single or odd-bounce scattering in the van Zyl decomposition. Cropland/natural vegetation and barren/sparsely vegetated land provide stronger single-bounce scattering (scattered from the soil beneath) than forest because more microwave energy penetrates the crown layer of them and interacts with the ground. The mean value of VanZyl3_Odd thus can be used for distinguishing forest from cropland/natural vegetation and barren/sparsely vegetated land. The mean value of VanZyl3_Vol is used to distinguish between cropland/natural vegetation and barren/sparsely vegetated land because the return scattered from the canopy of cropland/natural vegetation is more than that from barren/sparsely vegetated land.

Fig. 8 shows that no spatial feature was selected in the tree. This is because image objects are too fragmental to represent unbroken land parcels. To delineate the accurate boundaries of land parcels and retain subtle details, we used the small scale parameter to implement the image segmentation. However, the small scale parameter also led to an over segmentation of the image, resulting in a large number of fragmental objects. As shown in Fig. 7, some land parcels were segmented into many fragmental parts (image objects). An image object usually represents part of a land parcel; thus, using the spatial information on land parcels was difficult.

4. Results and discussion

4.1. Comparison between the proposed method and the Wishart supervised classification

A comparison between the proposed method and the Wishart supervised classification which is based on the coherency matrix (Lee et al., 1994; Pottier et al., 2005) was made to test the performance of the proposed method for LULC classification using RADARSAT-2 PolSAR data (Fig. 10). The Wishart supervised classification is commonly used for the classification of PolSAR data. This method is a pixel-based maximum likelihood classifier based on the complex Wishart distribution for the polarimetric coherency matrix. Using the confusion matrix that was determined using the validation set as basis, we calculated four statistics for the validation: overall accuracy (OA), estimate of kappa (Kappa), producer's accuracy (PA), and user's accuracy (UA) (Story & Congalton, 1986; Congalton & Green, 2009). The accuracy statistics of these two methods is provided in Tables 3 and 4. The overall accuracy of the proposed method was 86.64%, much higher than that of the Wishart supervised classification, which exhibited an overall accuracy of 69.66%. The kappa value of the proposed method was 0.84, whereas that of the Wishart supervised classification was 0.65. Moreover, the proposed method achieved higher producer's and user's accuracies for all the classes than did the Wishart supervised classification. The results show that a huge improvement was achieved using the proposed method compared with the Wishart supervised classification. However, it is still difficult to distinguish between lawn and barren/sparsely vegetated land using the proposed method. Lawn normally has higher soil moisture and more even surface than barren/sparsely vegetated land. Given that the single-bounce scattering from lawn and barren/sparsely vegetated land is greatly influenced by soil surface roughness and moisture content, the difference between lawn and barren/sparsely vegetated land can be characterized by RADARSAT-2 PolSAR images and used for distinguishing between them. However, some lawn fields have similar characteristics with barren/sparsely vegetated land because of the harvest of grass. It is therefore difficult to distinguish between lawn and barren/sparsely vegetated land when they are similar even and have similar soil moisture.

Although the comparison between the proposed method and the Wishart supervised classification indicates that the proposed method achieves much higher accuracies for LULC classification, it shows only the effects of using the whole four components, polarimetric decomposition, PolSAR interferometry, object-oriented image analysis, and decision tree algorithms. Additional comparisons were made to investigate the detailed contribution of these four components to LULC classification using RADARSAT-2 PolSAR data.

Author's personal copy

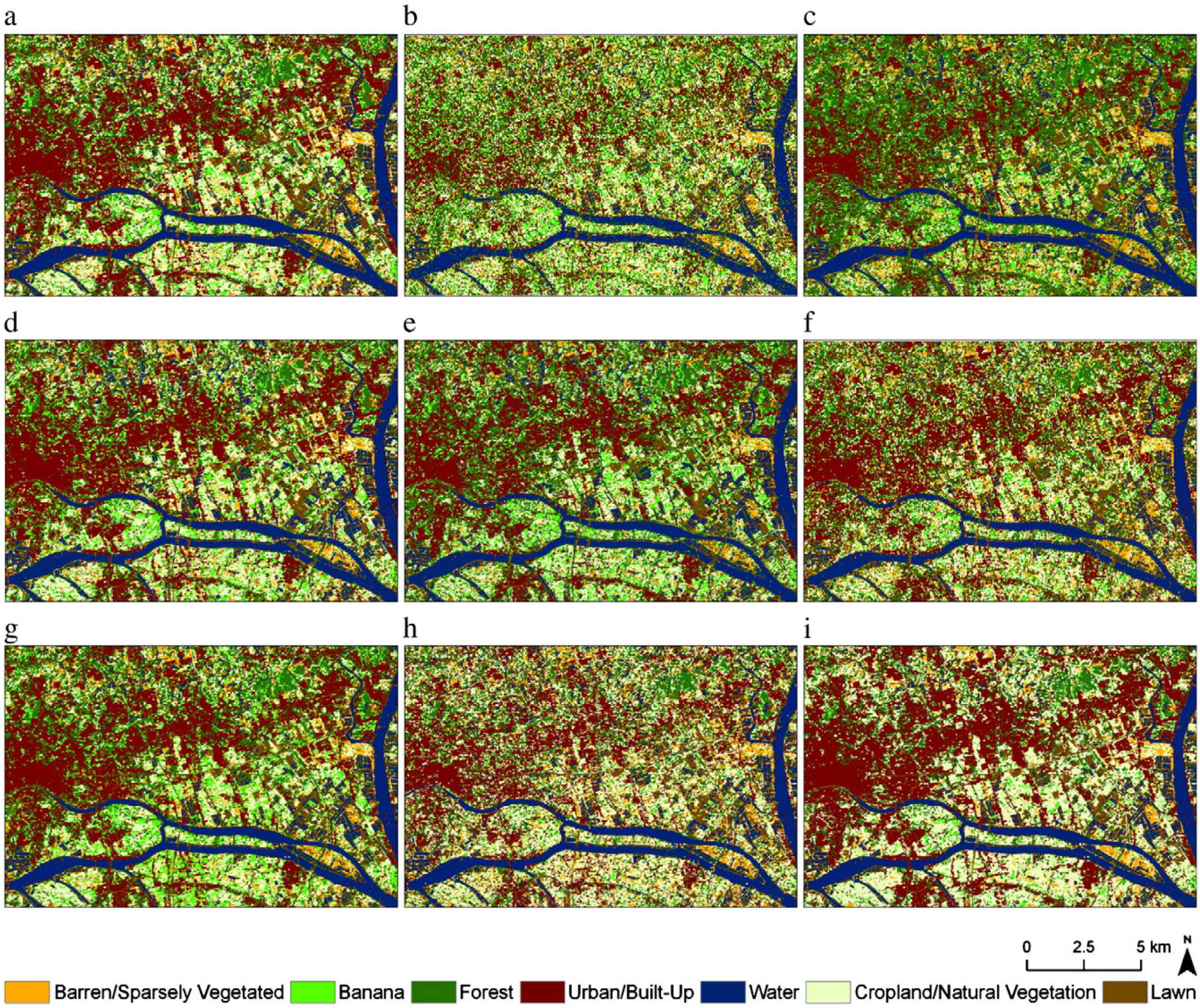

Fig. 10. LULC classification results (a) Proposed method, (b) Wishart supervised classification based on the coherency matrix, (c) Proposed method without polarimetric decomposition and PolSAR interferometry, (d) Proposed method without PolSAR interferometry, (e) Proposed method without polarimetric decomposition, (f) Proposed method without object-oriented image analysis, (g) Proposed method without incorporating textural and spatial information, (h) Proposed method using nearest neighbor classifiers instead of decision tree algorithms, (i) Proposed method using support vector classifiers instead of decision tree algorithms.

4.2. Contribution of the combination of polarimetric decomposition and PolSAR interferometry to LULC classification using RADARSAT-2 PolSAR data

The proposed method was used for the classification by only using object-oriented image analysis and decision tree algorithms without polarimetric decomposition and PolSAR interferometry. The classification was implemented based on the backscattering and coherency matrices, and the classification result and the accuracy evaluation are shown in Fig. 10c and Table 5. The comparison between the method without polarimetric decomposition and PolSAR interferometry and the method with the four components shows the contribution of the

Table 3
Classification accuracy of the proposed method.

Classified data	Reference data								
	B	UB	CN	BS	F	L	W	Total	UA (%)
B	7908	246	167	0	1102	0	0	9423	83.92
UB	0	8732	0	0	0	405	0	9137	95.57
CN	656	240	7249	454	461	0	0	9060	80.01
BS	0	0	0	5873	0	2861	0	8734	67.24
F	914	74	319	37	7132	0	0	8476	84.14
L	0	260	0	385	0	9226	0	9871	93.47
W	0	0	0	0	0	0	9542	9542	100.0
Total	9478	9552	7735	6749	8695	12,492	9542	64,243	
PA (%)	83.44	91.42	93.72	87.02	82.02	73.86	100.00		
OA (%)	86.64								
Kappa	0.84								

Author's personal copy

Table 4
Classification accuracy of the Wishart supervised classification based on the coherency matrix.

Classified data	Reference data								
	B	UB	CN	BS	F	L	W	Total	UA (%)
B	7438	694	395	0	896	0	0	9423	78.93
UB	1502	6244	139	1	857	263	131	9137	68.34
CN	873	536	5231	757	1663	0	0	9060	57.74
BS	0	18	317	5267	441	1510	1181	8734	60.30
F	1207	496	802	78	5526	367	0	8476	65.20
L	0	333	2	937	357	6032	2210	9871	61.11
W	0	0	0	2	6	521	9013	9542	94.46
Total	11,020	8321	6886	7042	9746	8693	12,535	64,243	
PA (%)	67.50	75.04	75.97	74.79	56.70	69.39	71.90		
OA (%)	69.66								
Kappa	0.65								

combination of polarimetric decomposition and PolSAR interferometry to LULC classification. The overall accuracy and the kappa value increased by 8.50% and 0.10 when polarimetric decomposition and PolSAR interferometry were used in this proposed method. Furthermore, the user's and producer's accuracies for almost all the classes improved when polarimetric decomposition and PolSAR interferometry were employed. The user's accuracies for cropland/natural vegetation, urban/built-up, and forest increased by 39.05%, 13.19%, and 10.95% respectively. The producer's accuracies for barren/sparsely vegetated land, forest, urban/built-up, and lawn increased by 16.00%, 15.62%, 8.93%, and 6.45% respectively.

As shown in Fig. 8, some polarimetric and polarimetric interferometric parameters are useful for identifying different vegetation types and distinguishing between vegetation and urban/built-up. Table 5 shows that cropland/natural vegetation tended to be confused with forest or barren/sparsely vegetated land in the classification without using polarimetric and polarimetric interferometric information. Fig. 8 shows that the mean values of VanZyl3_Odd, Freeman_Odd, and VanZyl3_Vol are useful in reducing the confusion. The mean values of VanZyl3_Odd and Freeman_Odd are important for distinguishing between cropland/natural vegetation and forest. The mean value of VanZyl3_Vol is helpful for separating cropland/natural vegetation from barren/sparsely vegetated land. In the classification without polarimetric and polarimetric interferometric information, forest in the shadow of mountains was always mistaken for lawn because there was minimal radar return from both of them (Fig. 11). The shadow of mountains was not illuminated by the sensor and the lawn reflected most of the incident radar wave to the opposite direction. Fig. 8 shows that the mean value of PH is helpful for differentiating forest in the shadow of mountains from lawn (Fig. 11). The mean value of Freeman_Odd is important for distinguishing between forest and banana. Table 5 shows that urban/built-up was always confused with some vegetation types, such as forest, banana, and cropland/natural vegetation. Fig. 8 shows that the mean values of Holm2_T_{22}, Krogager_KD, and γ_{opt_2} are crucial for reducing the confusion between these vegetation types and urban/built-up because all these parameters provide useful information for identifying urban/built-up areas (Fig. 9).

4.3. Contribution of polarimetric decomposition to LULC classification using RADARSAT-2 PolSAR data

This proposed method was conducted by using the components of polarimetric decomposition, object-oriented image analysis, and decision tree algorithms without PolSAR interferometry. The classification map and the accuracy evaluation are shown in Fig. 10d and Table 6. The comparison between this classification and the classification just using object-oriented image analysis and decision tree algorithms has demonstrated the importance of polarimetric decomposition for LULC classification. The overall accuracy and the kappa value increased by 6.39% and 0.08 when polarimetric parameters were used in the classification. The result shows that polarimetric parameters have significant implications for identifying different vegetation types and distinguishing between vegetation and urban/built-up. Moreover, polarimetric parameters are also helpful in distinguishing between water and lawn. However, the use of polarimetric parameters made banana prone to classification as urban/built-up and forest.

4.4. Contribution of PolSAR interferometry to LULC classification using RADARSAT-2 PolSAR data

This proposed method was implemented by using the components of PolSAR interferometry, object-oriented image analysis, and decision tree algorithms without polarimetric decomposition. The classification result and the accuracy evaluation are shown in Fig. 10e and Table 7. The comparison between this classification and the classification just using object-oriented image analysis and

Table 5
Classification accuracy of the proposed method without polarimetric decomposition and PolSAR interferometry.

Classified data	Reference data								
	B	UB	CN	BS	F	L	W	Total	UA (%)
B	8599	335	0	0	489	0	0	9423	91.26
UB	595	7527	0	0	610	405	0	9137	82.38
CN	738	597	3711	1974	2040	0	0	9060	40.96
BS	0	0	0	5873	0	2861	0	8734	67.24
F	693	406	308	37	6204	828	0	8476	73.19
L	0	260	0	385	0	9004	222	9871	91.22
W	0	0	0	0	0	260	9282	9542	97.28
Total	10,625	9125	4019	8269	9343	13,358	9504	64,243	
PA (%)	80.93	82.49	92.34	71.02	66.40	67.41	97.66		
OA (%)	78.14								
Kappa	0.74								

Author's personal copy

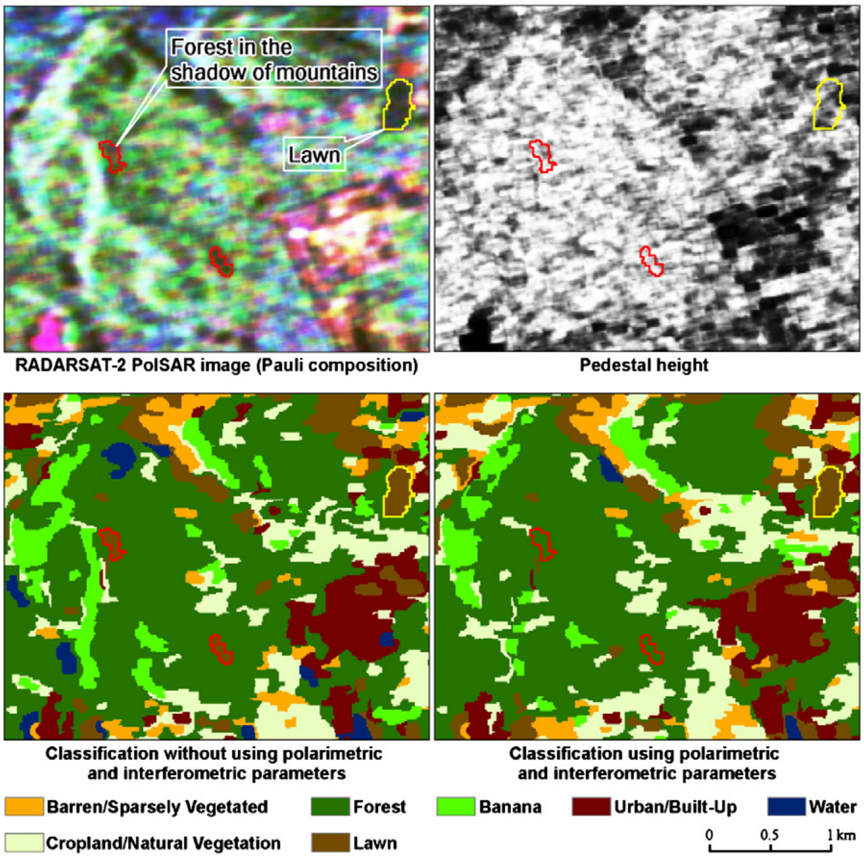

Fig. 11. Pedestal height is useful in reducing the confusion between forest in the shadow of mountains and lawn.

decision tree algorithms has demonstrated the contribution of PolSAR interferometry to LULC classification. The overall accuracy and the kappa value increased by 5.75% and 0.07 when polarimetric interferometric information was used in the classification. The result shows that polarimetric interferometric information is important for reducing a series of confusions, such as between urban/built-up and vegetation, between cropland/natural vegetation and barren/sparsely vegetated land, and between forest and other vegetation types (e.g. cropland/natural vegetation, banana, and lawn).

4.5. Contribution of object-oriented image analysis to LULC classification using RADARSAT-2 PolSAR data

The proposed method was carried out for the classification by using the components of polarimetric decomposition, PolSAR interferometry, and decision tree algorithms without object-oriented image analysis. The classification result and the accuracy evaluation are shown in Fig. 10f and Table 8. The comparison between the method without object-oriented image analysis and the method with the four components has demonstrated the importance of object-oriented image analysis for LULC classification. The overall accuracy and the kappa value increased by 9.99% and 0.11 when object-oriented image analysis was used in the classification. The user's and producer's accuracies for all the classes increased when object-oriented image analysis was used; however, the user's accuracy for barren/sparsely vegetated land exhibited a slight decrease. Moreover, the proposed method more effectively represented reality than did the pixel-based method. Lower spatial heterogeneity is observed in Fig. 10a than in Fig. 10f because the proposed method was less affected by speckle in the PolSAR images compared with the pixel-based method. This minimal effect was achieved through the implementation of the classification based on image objects.

The proposed method was implemented for the classification by using the four components without incorporating any textural or

Table 6
Classification accuracy of the proposed method without PolSAR interferometry.

Classified data	Reference data								
	B	UB	CN	BS	F	L	W	Total	UA (%)
B	7620	913	0	0	890	0	0	9423	80.87
UB	417	8315	0	0	0	405	0	9137	91.00
CN	656	290	7249	454	411	0	0	9060	80.01
BS	0	0	0	5873	0	2861	0	8734	67.24
F	1343	74	319	37	6703	0	0	8476	79.08
L	0	260	0	385	0	9004	222	9871	91.22
W	0	0	0	0	0	0	9542	9542	100.00
Total	10,036	9852	7568	6749	8004	12,270	9764	64,243	
PA (%)	75.93	84.40	95.78	87.02	83.75	73.38	97.73		
OA (%)	84.53								
Kappa	0.82								

Author's personal copy

Table 7
Classification accuracy of the proposed method without polarimetric decomposition.

Classified data	Reference data								
	B	UB	CN	BS	F	L	W	Total	UA (%)
B	8892	457	0	0	74	0	0	9423	94.36
UB	86	8646	0	0	0	405	0	9137	94.63
CN	751	326	6198	537	1248	0	0	9060	68.41
BS	0	0	0	5873	0	2861	0	8734	67.24
F	1289	268	308	37	5999	575	0	8476	70.78
L	0	0	0	385	260	9004	222	9871	91.22
W	0	0	0	0	0	260	9282	9542	97.28
Total	11,018	9697	6506	6832	7581	13,105	9504	64,243	
PA (%)	80.70	89.16	95.27	85.96	79.13	68.71	97.66		
OA (%)	83.89								
Kappa	0.81								

spatial feature (Fig. 10g). The accuracy evaluation of the classification is shown in Table 9. The comparison between the method without incorporating any textural or spatial feature and the proposed method shows the contribution of textural information to the final accuracy of LULC classification. The overall accuracy and the kappa value of the proposed method increased by 0.97% and 0.01 compared with the method in which textural information was not incorporated. Fig. 8 shows that the standard deviation of Freeman_Vol and the GLCM entropy of Yamaguchi3_Vol are helpful in distinguishing between water and lawn. In the field investigation, barren land plots were observed in some lawn fields because of the harvest of grass (Fig. 3), which makes lawn fields more heterogeneous than water in the PolSAR image. This should explain why water has GLCM entropy of Yamaguchi3_Vol lower than that of lawn.

The results show that object-oriented image analysis contributes substantially to the final accuracy of LULC classification using PolSAR data. Besides providing useful textural information to support the classification, another significant contribution of object-oriented image analysis is the reduction of the effect of the speckles in PolSAR images. Although the speckle filters were applied to the PolSAR images, the speckles still affected the classification results significantly. Besides the noise in backscattering and coherency matrices, there was large noise in some polarimetric or polarimetric interferometric parameters that were extracted later. As shown in Fig. 9, considerable noise can be observed in some polarimetric or polarimetric interferometric parameters, such as Holm2_T22, pedestal height, and γopt_2. The images of these parameters are too blurred to retain subtle details. In the pixel-based classification of PolSAR data, the speckles in PolSAR images have significant effect on the classification results. However, this problem can be minimized by using object-oriented image analysis. Such analysis can effectively reduce the speckle effect by extracting image objects from the Pauli composition image, which is good at retaining subtle details, and implementing classification based on image objects.

4.6. Contribution of decision tree algorithms to LULC classification using RADARSAT-2 PolSAR data

Classification using the proposed method integrating the nearest neighbor classifier (Baatz et al., 2004) instead of decision tree algorithms was carried out to investigate the contribution of decision tree algorithms to the final accuracy of LULC. The nearest neighbor classifier is a commonly used classification method for object-oriented classification. The features used in the nearest neighbor classification were selected using the Feature Space Optimization function embedded in Definiens Developer 7.0 (Baatz et al., 2004). The Feature Space Optimization compares the samples for selected classes with respect to features, and determines the combination of features that produces the largest average minimum distance between the samples of different classes. On the basis of the selected features, we implemented the nearest neighbor classification using Definiens Developer 7.0. The classification result and the accuracy evaluation are shown in Fig. 10h and Table 10. The overall accuracy and the kappa value of the classification using decision tree algorithms increased by 6.19% and 0.072 compared with the classification using the nearest neighbor classifier. Moreover, the experiment indicates that QUEST is more efficient than the Feature Space Optimization in feature selection.

Classification by integrating support vector machines (SVMs) (Vapnik, 1999) with the proposed method was also conducted instead of just integrating decision tree algorithms. SVMs are power classification tools that have been used widely, but the main limitation of SVMs is that they cannot automatically select features for classification. Irrelevant and redundant information usually contaminate the performance of SVM classifiers. Existing feature selection methods for a SVM classifier typically fall into two broad categories: wrappers and filters (Blum & Langley, 1997). Wrappers use a guided search, such as forward or backward selection, to methodically add or eliminate features one a time, and trying each resulting combination

Table 8
Classification accuracy of the proposed method without object-oriented image analysis.

Classified data	Reference data								
	B	UB	CN	BS	F	L	W	Total	UA (%)
B	7013	633	614	0	1163	0	0	9423	74.42
UB	278	8090	48	1	315	375	30	9137	88.54
CN	319	397	5974	1248	1122	0	0	9060	65.94
BS	0	20	145	6051	173	1882	463	8734	69.28
F	1017	275	791	105	5731	557	0	8476	67.61
L	0	248	0	830	173	7964	656	9871	80.68
W	0	1	0	1	2	1113	8425	9542	88.29
Total	8627	9664	7572	8236	8679	11,891	9574	64,243	
PA (%)	81.29	83.71	78.90	73.47	66.03	66.98	88.00		
OA (%)	76.66								
Kappa	0.73								

Author's personal copy

Table 9
Classification accuracy of the proposed method without incorporating textural and spatial information.

Classified data	Reference data								
	B	UB	CN	BS	F	L	W	Total	UA (%)
B	7908	246	167	0	1102	0	0	9423	83.92
UB	0	8732	0	0	0	405	0	9137	95.57
CN	656	240	6999	704	461	0	0	9060	77.25
BS	0	0	0	5701	0	2305	728	8734	65.27
F	914	74	319	37	7132	0	0	8476	84.14
L	0	260	0	158	0	9026	427	9871	91.44
W	0	0	0	0	0	0	9542	9542	100.00
Total	9478	9552	7485	6600	8695	11,736	10,697	64,243	
PA (%)	83.44	91.42	93.51	86.38	82.02	76.91	89.20		
OA (%)	85.67								
Kappa	0.83								

of features to determine which subset of features provide the best classification performance when used with the chosen classifier. Given that wrappers use the prediction performance of the particular learning algorithm used, they often give better results than filters. Therefore, in this work, a genetic algorithm based wrapper feature selection method was implemented using the Weka 3.6 software (Witten, et al., 2011) to select features. LibSVM (Chang & Lin, 2011) was used to implement SVM classification based on the selected features. The classification result and the accuracy evaluation are shown in Fig. 10i and Table 11. The result shows that the accuracy of the SVM classification is similar with that of the decision tree algorithm. Although the SVM classification achieved a little higher overall accuracy than the decision tree algorithm, the decision tree algorithm is more efficient to select features and implement classification. Wrapper approaches are computationally expensive, as they require the classifier to be trained and evaluated a large number of times with different subsets of features. Furthermore, the decision tree algorithm can provide clear classification rules that can be easily interpreted based on the physical meaning of the features used in the classification. This is very helpful in providing physical insight for LULC classification using PolSAR data.

5. Conclusions

This paper has proposed a new four-component method that integrates polarimetric decomposition, PolSAR interferometry, object-oriented image analysis, and decision tree algorithms for LULC classification using RADARSAT-2 PolSAR data. The comparison between the proposed method and the Wishart supervised classification which is based on the coherency matrix was made to test their performance for LULC classification. The analysis shows that the proposed method can significantly improve the overall accuracy and kappa value of the Wishart supervised classification by 16.98% and 0.19. Moreover, the user's and producer's accuracies for all the LULC classes can be improved using the proposed method compared with the Wishart supervised classification. The results indicate that the proposed method performs much better than does the Wishart supervised classification for LULC classification using RADARSAT-2 PolSAR data.

Polarimetric parameters extracted using different polarimetric decomposition methods are related to the scattering properties of the observed objects; thus, they have significant implications for the classification of PolSAR data. The overall accuracy and the kappa value of LULC classification can be improved by 6.39% and 0.08 if polarimetric parameters are used in the classification. This study has shown that some polarimetric parameters are important in identifying different vegetation types and distinguishing between vegetation and urban/built-up. VanZyl3_Odd and Freeman_Odd are important in distinguishing between cropland/natural vegetation and forest. VanZyl3_Vol is useful for distinguishing between cropland/natural vegetation and barren/sparsely vegetated land. PH can be used to reduce the confusion between forest in the shadow of mountains and lawn. Freeman_Odd is helpful in distinguishing between forest and barren/sparsely vegetated land. Holm2_T_{22} and Krogager_KD are important in reducing the confusion between urban/built-up and vegetation.

PolSAR interferometry can be used to extract useful polarimetric interferometric information to support LULC classification. This study has shown that the polarimetric interferometric information extracted from the repeat-pass RADARSAT-2 images is important in reducing the confusion between urban/built-up and vegetation, such as banana trees, forest, and cropland/natural vegetation, that between cropland/natural vegetation and barren/sparsely vegetated land, and that between forest and banana trees. The overall accuracy and kappa value of LULC classification can be improved by 5.75% and 0.07 if polarimetric interferometric information is used in the classification. Moreover, the combination of polarimetric and polarimetric interferometric information can significantly improve the overall accuracy and kappa value of LULC classification by 8.50% and 0.10.

Table 10
Classification accuracy of the proposed method using the nearest neighbor classifier instead of decision tree algorithms.

Classified data	Reference data								
	B	UB	CN	BS	F	L	W	Total	UA (%)
B	6491	420	921	0	1591	0	0	9423	68.88
UB	321	7138	121	0	1152	214	191	9137	78.12
CN	0	240	7893	589	338	0	0	9060	87.12
BS	0	0	242	6239	0	1060	1193	8734	71.43
F	0	244	1269	157	6260	37	509	8476	73.86
L	0	0	0	975	0	8122	774	9871	82.28
W	0	0	0	0	0	0	9542	9542	100.00
Total	6812	8042	10,446	7960	9341	9433	12,209	64,243	
PA (%)	95.29	88.76	75.56	78.38	67.02	86.10	78.16		
OA (%)	80.45								
Kappa	0.77								

Author's personal copy

Table 11
Classification accuracy of the proposed method using SVM instead of decision tree algorithms.

Classified data	Reference data								
	B	UB	CN	BS	F	L	W	Total	UA (%)
B	7403	246	483	0	1291	0	0	9423	78.56
UB	0	8732	0	0	0	214	191	9137	95.57
CN	126	290	8053	241	350	0	0	9060	88.89
BS	0	0	43	6295	0	2396	0	8734	72.07
F	731	74	763	0	6908	0	0	8476	81.50
L	0	0	0	385	0	9059	427	9871	91.77
W	0	0	0	0	0	0	9542	9542	100.00
Total	8260	9342	9342	6921	8549	11,669	10,160	64,243	
PA (%)	89.62	93.47	86.20	90.96	80.80	77.63	93.92		
OA (%)	87.16								
Kappa	0.85								

Object-oriented image analysis is very helpful in improving the accuracy of the classification of PolSAR data by reducing the effect of speckle in PolSAR images and extracting more information for the classification. The overall accuracy and kappa value of object-oriented classification of PolSAR data increased by 9.99% and 0.11 compared with those of conventional pixel-based classification. Speckle in PolSAR images has a significant effect on the accuracy of the classification of PolSAR data. Object-oriented image analysis can effectively reduce the speckle effect by implementing classification based on image objects. Furthermore, the object-oriented classification of PolSAR data exhibited better performance in terms of representing reality than did the pixel-based classification because it was less affected by speckle. The textural information in PolSAR images is helpful in enhancing the accuracy of the classification of PolSAR data. The study has indicated that the standard deviation of Freeman_Vol and the GLCM entropy of Yamaguchi3_Vol are helpful in distinguishing between water and lawn.

With the addition of polarimetric, interferometric, textural, and spatial information, hundreds of features can be potentially incorporated into the classification of PolSAR data. Decision tree algorithms proved to be efficient in selecting features and implementing classification. The decision tree algorithm can achieve higher classification accuracy than the nearest neighbor classification implemented using Definiens Developer 7.0, and the overall accuracy of the decision tree algorithm is similar with that of the support vector classification which is implemented based on the features selected using genetic algorithms. Compared with the nearest neighbor and support vector classification, the decision tree algorithm is more efficient to select features and implement classification. Furthermore, the decision tree algorithm can provide clear classification rules that can be easily interpreted based on the physical meaning of the features used in the classification. This is very helpful in providing physical insight for LULC classification using PolSAR data.

The main contribution of the interferometric information extracted from the repeat-pass RADARSAT-2 PolSAR images (24 days time interval) is reducing the confusion between urban/built-up and vegetation. The interferometric information extracted from PolInSAR images with short time interval should have more contribution to the separation of different vegetation because the magnitude of interferometric coherency, which is less affected by any amplitude saturation effects, allows high biomass forest classification even at higher frequencies (Li et al., 2009). Further studies will be conducted to incorporate this kind of interferometric information into the classification of PolSAR data to achieve more observation space and higher accuracy.

The segmentation of PolSAR images remains a challenge for the object-oriented classification of PolSAR data. Although multi-resolution segmentation implemented on the Pauli RGB composition image can delineate the accurate boundaries of land parcels and retain subtle details, it creates a huge number of image objects, which are too fragmental to represent unbroken land parcels. This makes the utilization of spatial information of land parcels difficult. Further studies need to be conducted to improve segmentation methods for PolSAR images.

Acknowledgments

This study was supported by the National Basic Research Program of China (973 Program) (Grant No. 2011CB707103), the Key National Natural Science Foundation of China (Grant No. 40830532), and the Science and Operational Applications Research for RADARSAT-2 Program (SOAR 2762). The authors would like to thank the Canadian Space Agency (CSA) and the MDA GEOSPATIAL SERVICES INC. for providing the RADARSAT-2 data.

References

Alberga, V. (2007). A study of land cover classification using polarimetric SAR parameters. *International Journal of Remote Sensing*, *28*, 3851–3870.

Baatz, M., Benz, U., Dehghani, S., Heynen, M., Höltje, A., Hofmann, P., Lingenfelder, I., Mimler, M., Sohlbach, M., & Weber, M. (2004). *eCognition professional user guide 4.* Munich: Definiens Imaging.

Barnes, R. M. (1988). Roll-invariant decompositions for the polarization covariance matrix. *Proceedings of Polarimetry Technology Workshop, Redstone Arsenal, AL.*

Barnes, C. F., & Burki, J. (2006). Late-season rural land-cover estimation with polarimetric-SAR intensity pixel blocks and sigma-tree-structured near-neighbor classifiers. *IEEE Transactions on Geoscience and Remote Sensing*, *44*, 2384–2392.

Benz, U. C., Hofmann, P., Willhauck, G., Lingenfelder, I., & Heynen, M. (2004). Multi-resolution, object-oriented fuzzy analysis of remote sensing data for GIS-ready information. *ISPRS Journal of Photogrammetry and Remote Sensing*, *58*, 239–258.

Blum, A. L., & Langley, P. (1997). Selection of relevant features and examples in machine learning. *Artificial Intelligence*, *97*, 245–271.

Borghys, D., Yvinec, Y., Perneela, C., Pizurica, A., & Philips, W. (2006). Supervised feature-based classification of multi-channel SAR images. *Pattern Recognition Letters*, *27*, 252–258.

Cameron, W. L., & Rais, H. (2006). Conservative polarimetric scatterers and their role in incorrect extensions of the Cameron decomposition. *IEEE Transactions on Geoscience and Remote Sensing*, *44*, 3506–3516.

Chang, C. C., & Lin, C. J. (2011). LIBSVM: A library for support vector machines. *ACM Transactions on Intelligent Systems and Technology*, *2*(27) 1–27:27. Software available at http://www.csie.ntu.edu.tw/~cjlin/libsvm.

Chen, K. S., Huang, W. P., Tsay, D. H., & Amar, F. (1996). Classification of multifrequency polarimetric SAR imagery using a dynamic learning neural network. *IEEE Transactions on Geoscience and Remote Sensing*, *34*, 814–820.

Cloude, S. R. (1985). Target decomposition-theorems in radar scattering. *Electronics Letters*, *21*, 22–24.

Cloude, S. R., & Pottier, E. (1996). A review of target decomposition theorems in radar polarimetry. *IEEE Transactions on Geoscience and Remote Sensing*, *34*, 498–518.

Cloude, S. R., & Pottier, E. (1997). An entropy based classification scheme for land applications of polarimetric SAR. *IEEE Transactions on Geoscience and Remote Sensing*, *35*, 68–78.

Congalton, R., & Green, K. (2009). *Assessing the accuracy of remotely sensed data: principles and practices.* Boca Raton: CRC Press.

Crawford, M. M., Kumar, S., Ricard, M. R., Gibeaut, J. C., & Neuenschwander, A. (1999). Fusion of airborne polarimetric and interferometric SAR for classification of coastal environments. *IEEE Transactions on Geoscience and Remote Sensing*, *37*, 1306–1315.

Du, L., & Lee, J. S. (1996). Fuzzy classification of earth terrain covers using complex polarimetric SAR data. *International Journal of Remote Sensing*, *17*, 809–826.

Durden, S. L., Vanzyl, J. J., & Zebker, H. A. (1990). The unpolarized component in polarimetric radar observations of forested areas. *IEEE Transactions on Geoscience and Remote Sensing*, *28*, 268–271.

Author's personal copy

Ferro-Famil, L., Pottier, E., & Lee, J. S. (2001). Unsupervised classification of multifrequency and fully polarimetric SAR images based on the H/A/alpha-Wishart classifier. *IEEE Transactions on Geoscience and Remote Sensing*, *39*, 2332–2342.

Freeman, A., & Durden, S. L. (1998). A three-component scattering model for polarimetric SAR data. *IEEE Transactions on Geoscience and Remote Sensing*, *36*, 963–973.

Freeman, A. (2007). Fitting a two-component scattering model to polarimetric SAR data from forests. *IEEE Transactions on Geoscience and Remote Sensing*, *45*, 2583–2592.

Freitas, C. D., Soler, L. D., Anna, S. J. S. S., Dutra, L. V., dos Santos, J. R., Mura, J. C., & Correia, A. H. (2008). Land use and land cover mapping in the Brazilian Amazon using polarimetric airborne p-band SAR data. *IEEE Transactions on Geoscience and Remote Sensing*, *46*, 2956–2970.

Friedl, M. A., & Brodley, C. E. (1997). Decision tree classification of land cover from remotely sensed data. *Remote Sensing of Environment*, *61*, 399–409.

Gamba, P., & Houshmand, B. (1999). Three-dimensional road network by fusion of polarimetric and interferometric SAR data. *Proceedings of 1999 IEEE International Geoscience and Remote Sensing Symposium* (pp. 302–304). Germany: Hamburg.

Gao, Y., Mas, J. F., Maathuis, B. H. P., Zhang, X. M., & Van Dijk, P. M. (2006). Comparison of pixel-based and object-oriented image classification approaches — A case study in a coal fire area, Wuda, Inner Mongolia, China. *International Journal of Remote Sensing*, *27*, 4039–4055.

Geneletti, D., & Gorte, B. G. H. (2003). A method for object-oriented land cover classification combining Landsat TM data and aerial photographs. *International Journal of Remote Sensing*, *24*, 1273–1286.

Holm, W. A., & Barnes, R. M. (1988). On radar polarization mixed state decomposition theorems. *Proceedings of the 1988 USA National Radar Conference* (pp. 20–21). MI, USA: Ann Arbor.

Huynen, J. R. (1970). *Phenomenological theory of radar targets (PhD dissertation)*. Rotterdam: Drukkerij Bronder-offset N. V.

Krogager, E. (1990). New decomposition of the radar target scattering matrix. *Electronics Letters*, *26*, 1525–1527.

Laliberte, A. S., Koppa, J., Fredrickson, E. L., & Rango, A. (2006). Comparison of nearest neighbor and rule-based decision tree classification in an object-oriented environment. *Proceedings of 2006 IEEE International Geoscience and Remote Sensing Symposium* (pp. 3923–3926). Denver, Colorado.

Lawrence, R. L., & Wright, A. (2001). Rule-based classification systems using classification and regression tree (CART) analysis. *Photogrammetric Engineering and Remote Sensing*, *67*, 1137–1142.

Lee, J. S., Grunes, M. R., & Kwok, R. (1994). Classification of multi-look polarimetric SAR imagery-based on complex Wishart distribution. *International Journal of Remote Sensing*, *15*, 2299–2311.

Lee, J. S., Grunes, M. R., Ainsworth, T. L., Du, L. J., Schuler, D. L., & Cloude, S. R. (1999). Unsupervised classification using polarimetric decomposition and the complex Wishart classifier. *IEEE Transactions on Geoscience and Remote Sensing*, *37*, 2249–2258.

Lee, J. S., Grunes, M. R., & de Grandi, G. (1999). Polarimetric SAR speckle filtering and its implication for classification. *IEEE Transactions on Geoscience and Remote Sensing*, *37*, 2363–2373.

Lee, J. S., Grunes, M. R., & Pottier, E. (2001). Quantitative comparison of classification capability: Fully polarimetric versus dual and single-polarization SAR. *IEEE Transactions on Geoscience and Remote Sensing*, *39*, 2343–2351.

Lee, J. S., & Pottier, E. (2009). *Polarimetric radar imaging from basics to applications.* New York: CRC Press.

Li, X., & Yeh, A. G. (2004). Multitemporal SAR images for monitoring cultivation systems using case-based reasoning. *Remote Sensing of Environment*, *90*, 524–534.

Li, H. T., Gu, H. Y., Han, Y. S., & Yang, J. H. (2008). Object-oriented classification of polarimetric SAR imagery based on statistical region merging and support vector machine. *Proceedings of the 2008 International Workshop on Earth Observation and Remote Sensing Applications* (pp. 147–152). Beijing, China.

Li, X., Yeh, A. G. O., Qian, J. P., Ai, B., & Qi, Z. X. (2009). A matching algorithm for detecting land use changes using case-based reasoning. *Photogrammetric Engineering and Remote Sensing*, *75*, 1319–1332.

Lim, T. S., Loh, W. Y., & Shih, Y. S. (2000). A comparison of prediction accuracy, complexity, and training time of thirty-three old and new classification algorithms. *Machine Learning*, *40*, 203–228.

Loh, W. Y., & Shih, Y. S. (1997). Split selection methods for classification trees. *Statistica Sinica*, *7*, 815–840.

López-Martínez, C., Ferro-Famil, L. & Pottier, E. (2005). PolSARpro v4.0 Polarimetry Tutorial, URL: http://earth.esa.int/polsarpro/tutorial.html, European Space Agency, Paris, France.

McCoy, R. M. (2005). *Field methods in remote sensing.* New York: The Guilford Press.

McIver, D. K., & Friedl, M. A. (2002). Using prior probabilities in decision-tree classification of remotely sensed data. *Remote Sensing of Environment*, *81*, 253–261.

Neumann, M., Ferro-Famil, L., & Pottier, E. (2009). A general model-based polarimetric decomposition scheme for vegetated areas. *Proceedings of POLINSAR'09, Frascati, Italy*.

Papathanassiou, K. P., & Cloude, S. R. (2001). Single-baseline polarimetric SAR interferometry. *IEEE Transactions on Geoscience and Remote Sensing*, *39*, 2352–2363.

Pierce, L. E., Ulaby, F. T., Sarabandi, K., & Dobson, M. C. (1994). Knowledge-based classification of polarimetric SAR images. *IEEE Transactions on Geoscience and Remote Sensing*, *32*, 1081–1086.

Pierce, L. E., Bergen, K. M., Dobson, M. C., & Ulaby, F. T. (1998). Multitemporal land-cover classification using SIR-C/X-SAR imagery. *Remote Sensing of Environment*, *64*, 20–33.

Pottier, E., & Lee, J. S. (2000). Application of the "H/A/(alpha)under-bar" polarimetric decomposition theorem for unsupervised classification of fully polarimetric SAR data based on the Wishart distribution. *roceedings of CEOS SAR Workshop* (pp. 335–340). Toulouse, France.

Pottier, E., J.S. Lee, & Ferro-Famil, L. (2005). *PolSARpro v3.0 Lecture Notes — Advanced concepts*. URL: http://earth.esa.int/polsarpro/tutorial.html, European Space Agency, Paris, France.

Rignot, E., Chellappa, R., & Dubois, P. (1992). Unsupervised segmentation of polarimetric SAR data using the covariance-matrix. *IEEE Transactions on Geoscience and Remote Sensing*, *30*, 697–705.

Roberts, D. A., Keller, M., & Soares, J. V. (2003). Studies of land-cover, land-use, and biophysical properties of vegetation in the large scale biosphere atmosphere experiment in Amazonia. *Remote Sensing of Environment*, *87*, 377–388.

Saatchi, S. S., Soares, J. V., & Alves, D. S. (1997). Mapping deforestation and land use in Amazon rainforest by using SIR-C imagery. *Remote Sensing of Environment*, *59*, 191–202.

Shimoni, M., Borghys, D., Heremans, R., Perneel, C., & Acheroy, M. (2009). Fusion of PolSAR and PolInSAR data for land cover classification. *International Journal of Applied Earth Observation and Geoinformation*, *11*, 169–180.

Story, M., & Congalton, R. G. (1986). Accuracy assessment — A user's perspective. *Photogrammetric Engineering and Remote Sensing*, *52*, 397–399.

Swain, P. H., & Hauska, H. (1977). Decision tree classifier — Design and potential. *IEEE Transactions on Geoscience and Remote Sensing*, *15*, 142–147.

Thenkabail, P. S., Schull, M., & Turral, H. (2005). Ganges and Indus river basin land use/land cover (LULC) and irrigated area mapping using continuous streams of MODIS data. *Remote Sensing of Environment*, *95*, 317–341.

Touzi, R. (2007). Target scattering decomposition in terms of roll-invariant target parameters. *IEEE Transactions on Geoscience and Remote Sensing*, *45*, 73–84.

Ulaby, F. T., Kouyate, F., Brisco, B., & Williams, T. H. L. (1986). Textural information in SAR images. *IEEE Transactions on Geoscience and Remote Sensing*, *24*, 235–245.

Vapnik, V. (1999). *The nature of statistical learning theory.* New York: Springer.

Vanzyl, J. J. (1993). Application of Cloude target decomposition theorem to polarimetric imaging radar data. *Radar Polarimetry*, *1748*, 184–191.

Watts, J. D., Lawrence, R. L., Miller, P. R., & Montagne, C. (2009). Monitoring of cropland practices for carbon sequestration purposes in north central Montana by Landsat remote sensing. *Remote Sensing of Environment*, *113*, 1843–1852.

Witten, I. H., Frank, E., & Hall, M. A. (2011). *Data mining: Practical machine learning tools and techniques.* Burlington, MA: Morgan Kaufmann.

Yamaguchi, Y., Moriyama, T., Ishido, M., & Yamada, H. (2005). Four-component scattering model for polarimetric SAR image decomposition. *IEEE Transactions on Geoscience and Remote Sensing*, *43*, 1699–1706.

Yang, J., Yamaguchi, Y., Yamada, H., Sengoku, M., & Lin, S. M. (1998). Stable decomposition of Mueller matrix. *IEICE Transactions on Communications*, 1261–1268 E81b,.

Yeh, A. G. O., & Li, X. (1996). Urban growth management in the Pearl River Delta — An integrated remote sensing and GIS approach. *ITC Journal*, *1*, 77–86.